Republic of Iraq

Ministry of Higher Education and Scientific Research
University of Diyala
College of Science
Department of Physics

Improving the properties of magnetic nano particles (Co_Ni) ferrite by pulsed laser deposition and study its biological effect.

A Thesis
Submitted to the Council of the College of Science- University of Diyala in Partial Fulfillment of the Requirements for the Degree of Master of Science in Physics

By

Marwa Hazem Sabbar

B. Sc. in Physics (2019)

Supervised By

Prof. Dr.
Tahseen H. Mubarak

Assist. Prof. Dr.
Nada S. Ahmed

2022 AD

1444AH

بسم الله الرحمن الرحيم

(قَالُوا سُبْحَانَكَ لا عِلْمَ لَنَا إِلَّا مَا عَلَّمْتَنَا إِنَّكَ أَنْتَ الْعَلِيمُ الْحَكِيمُ﴿ ٣٢ ﴾)

صدق الله العظيم

سورة البقرة-الآية ٣٢

Dedication

First of all I thank his Almighty Allah, whose Grace enabled me to continue this work and overcome all difficulties

And

To.....

My Parents father and mother

To.....

My brother

To.....

My Friends

To.....

The people who love and supported me all the time

Acknowledgement

First and foremost, I would like to thank Almighty Allah for giving me the strength, knowledge, ability and opportunity to undertake, persevere and complete this research. Without his blessings, this achievement would not have been possible.

There are many people I need to thank for their support and encouragement.

I would like to express my heartfelt thanks to my supervisors,

Prof. Dr. Tahseen H. Mubarak and ***Assist. Prof. Dr. Nada S. Ahmed,*** for their guidance, inspiration, and encouragement. I am very grateful for both their expertise and commitments throughout the course of my research.

I express my thanks to head of Physics Department ***Asst. Prof. Dr. Ammar A. Habeeb*** and all members, especially prof. Dr. Ziad T. Khodiar, Prof. Dr. Nabeel A. Bakr and Prof. Dr. Sabah A. Salman for their cooperation.

It certainly would have been very difficult completing this research without the support from ***my parents and my brother.*** Their encouragements and supports inspired me to hold out to the end.

I am also grateful to the Physics Department, College of Science at Baghdad University, especially *Dr. Falah A-H.Mutlak* for their kind help during the laboratory work

My thanks and appreciation are to due those who helped me with the words or the work of my professors and brothers students, at the University of Diyala .

researcher

Contents

List of Figures

List of Tables

List of symbols

Symbols	Description	Units
d_{hkl}	Inter-atomic distances	nm
hkl	Miller indices	nm
D	Crystalline size	nm
h	Planck constant	J/s
Θ	Diffraction angle	Degree
λ	Wavelength	nm

List of Abbreviations

Abbreviations	Definition
NPs	Nanoparticles
XRD	X-ray diffraction
FWHM	Full width at half maximum
TEM	Transmission electron microscopy
FT-IR	Fourier transform infrared spectroscopy
SEM	Scanning electron microscopy
FE-SEM	Field emission-scanning electron microscopes

VSM	Vibrating sample magnetometer
MRI	Magnetic resonance imaging
FWHM	Full width at half-maximum
PXRD	Powder X-ray diffraction
GMR	Giant magneto resistance
PLD	Pulse Laser Depostion
MHA	Mueller Hinton Agar
RFA	Radio frequency ablation
MNPs	Micronized nanoparticals
MR	Magmatic Recording
MMONPs	magnetic metal oxide nanoparticles

.

ABSTRACT:

In this research, we prepared magnetic nano particles in format $Co_{1-x}Ni_x Fe_2 O_4$ in two methods. The first method is Co-precipitationnand were used pulsed laser deposition (PLD).

We used a mixture of nickel nitrate, cobalt nitrate, iron nitrate, as well as sodium hydroxide as a chelating agent to balance the ratio of the oxidizing agent.

The ferrite NPs were calcined at temperatures (300 °C) for 3 hr. to remove water content and unwanted impurities and to obtain a better single-phase spinel structure. The resulting powder is then compressed into a disc with a diameter of (2 cm) and then we use laser deposition technology to obtain thin film.

Structure and magnetic properties of the NPs were tested using XRD, FE-SEM, FTIR, and finally the Vibrating Sample Magnetometer (VSM), which revealed the presence of Super para magnetic samples. The x-ray spectrum shows that the pattern of the particles formed is of the face -centered cubic and the theoretical values of the lattice constant and crystalline size (D) were calculated .The crystalline size calculated was located in the range (22.6-26.6 nm), either in the pulsed laser deposition method in the range (13.7)nm, which reflects the highly crystalline nature of these nanoparticles. The FTIR spectrum shows two absorption bands ranging between 400 and 600 cm^{-1}. These bands indicated that the composition of the spectrum for all the samples is ferrite.

The Field emission scanning electron microscopes (FE-SEM) images confirmed that the preparation methods produced spherical nanoparticles with a slight change in the particle size distribution. The average particle size by co-precipitation had estimated to be about 23 nm and the average particle size by pulsed laser deposition(PLD) method had estimated to be about 20 nm.

The magnetic properties vibrating sample magnetometer (VSM) showed good correlation with the structural parameters of the spinal structure, which increased with the Ni content.

When using nanoparticles prepared by co-precipitation method on *Escherichia coli and Streptococcus* bacteria, the highest inhibition zone ranged from (27-33) mm. When using nanoparticles prepared by using the method of pulsd laser deposition on the same types of bacteria, *(S.aureus)*was found to have the highest inhibition zone (22-32) mm , while Bacteria(*Escherichia coli*) the inhibition zone (27-30) mm.

Chapter One

Introduction And Literature Review

1.1 Introduction

Nanoparticles (NPs) are defined as objects with a size less than (100 nm). It can be categorized according to its size and diameters. Mainly, they are classified into compact materials and nanodispersions [1].

The possibility of using nanostructured materials for a wide range of super performant technological applications is of particular interest for scientific research and medical applications [2].

One of the most significant groups of magnetically distinct nanomaterials is magnetic nanoparticles (MNPs). High field irreversibility, a large saturation zone, Superparamagnetism, additional anisotropy, temperature-dependent hysteresis, etc., are among the most notable properties of magnetic nanoparticles [3].

The magnetic nanoparticles for bio-applications have piqued the interest of researchers due to their compact dimensions to the biological entities and unique magnetic properties. Even though most living organisms consist of cells that are around ten μm in size, typically, the dimensions of a cell are measured in nanometers. For example, the dimensions of genes are (10–100) nm in length and 2 nm in width, proteins range in size from(5 – 50) nm, while viruses are(20 – 450) nm [4].

Hilbert first thought of the possibility of collecting high electrical resistivity of the oxides with magnetic properties wanted in terms of magnetic material be appropriate to practice for high frequencies were the result of research in this direction discovery of ferrite [5]. Ferrites with spinel structure represent the important class of magnetic materials consisting of ferric oxide and metal oxides. The spinel ferrites have widely studied the result of their numerous applications in several fields. The

spinel ferrite has the chemical formula MFe_2O_4, where M is a divalent metal ion such as Co, Ni, Mn, etc. While still maintaining the spine structure [6]. Ferrites are ceramic, homogeneous materials composed of various oxides with iron oxide as their main constituent. Depending on the magnetic properties, ferrites can be categorized as “soft” and “hard” ferrite. Soft ferrites have low coercivity, while hard ferrites have high coercivity. Hard ferrite has high coercivity, and moderate magnetization coercivity stands for the resistance to getting demagnetized for removal of the applied field, which satisfies it for being a permanent magnet [7].

Magnetic nanomaterials have a tremendous scientific and technological impact. $CoFe_2O_4$ and $NiFe_2O_4$ are interesting magnetic materials with reverse. The ferrite nickel spinel structure is a soft magnetic material with high electrical resistance, useful for high-frequency applications, such as transformers. The ability to control magnetic properties such as The saturation magnetization, residual magnetization and coercivity of these ferrite nanostructures are essential not only to get a basic understanding of magnetism in these necessary materials but also for their applications such as magnetism Contrast-enhancing factors in resonance imaging in Magnetic hyperthermia for the biomedical therapeutic purpose [8].

Spinel ferrite is a class of oxide materials with remarkable electrical and magnetic properties, which have been investigated and applied during the last few decades. Among all inverse spinel ferrites, the nickel substituted cobalt ferrite has been extensively studied because of their good chemical and thermal stability, high electrical resistivity, magnetic anisotropy, high coercivity, and coercivity and moderate saturation magnetization, various exchange interactions and super-paramagnetism etc. In addition to

these, they exhibit ferrimagnetism, originating from the magnetic moment of anti-parallel spins between Fe^{3+} ions at tetrahedral sites and Co^{2+} or Ni^{2+} ions at octahedral sites [9]. Due to the magnetic properties. Cobalt ferrite ($CoFe_2O_4$) is a popular hard magnetic material because of its high magnetism and coercive strength (Ms). $CoFe_2O_4$ nanoparticles have several applications in industry and biology due to their remarkable physical and chemical stability [10].

1.2. Literature Review

M.S Khandekar et al., (2011) Cobalt ferrite's structural and electrical properties were investigated to determine the impact of temperature. X-ray diffraction spectroscopy was used to examine the samples' structures after they were synthesized at temperatures of (700-800-900). (XRD) results demonstrated that particle size increases with temperature. FTIR spectroscopy examinations, the particles show the tetrahedral and octahedral phases [11].

R.Lotfi et al., (2012) studied the effect of temperature on the preparation of nickel-compensated cobalt ferrite by the co-precipitation method, where the nanoparticles were prepared, and the impact of temperature on particle sizes was studied. By exposing them to temperatures (600-900) °C, the structural properties of the particles were studied through XRD, which showed that the particle size ranged between (22-38 nm) and from SEM measurements. The surface had an important role in the particle formation phase and showed the formation of a single crystalline cubic phase at pH 11 [12].

Maheshkumar L. Mane et al., (2013) Nd: YAG laser irradiation effect on the structural and magnetic properties of Cobalt–Iron oxides were studied in the $CoFe_2O_4$ ferrite composition. $CoFe_2O_4$ spinel ferrite was prepared by the conventional double sintering ceramic method. On irradiation by Nd: YAG laser beam, significant changes in the hysteresis loop features are observed. This may be attributed to the formation of defects in the samples due to irradiation [13].

M. Mozaffari et al., (2014) Nickel substituted cobalt ferrite $Ni_xCo_{1-x}Fe_2O_4$ (x=0.1, 0.3, 0.5, 0.7, and 0.9) was synthesized as nanoparticles through Sol-gel synthesis. With the help of X-ray diffraction, we could establish that the samples' crystallite size was around (30 nm). Images from a scanning electron microscope showed that particles averaged between 70 and 160 nm in size, suggesting that crystallites are packed densely within each molecule. The lattice parameter of the specimens declined from 8.350 to 8.300 as the nickel concentration rose. Saturation magnetization was measured to be between 70.8 and 37.3 emu/g, and this value decreased with increasing nickel content [14].

Muhammad et al ., (2014) The co-precipitation method synthesizes ferrites, resulting in a refined crystal structure. We present the first report of pre-digestion irradiation of spinel ferrite utilizing a pulsed Nd: YAG (1064 nm) laser to improve the structure of this material. They considered the significance of Co–Zn ferrite particles in technology requiring a single phase. XRD and TEM studies showed that predigestion laser irradiation of ferrite solution decreased the number of unwanted peaks and altered the average crystallite size. When exposed to a laser, the average size of ferrite particles shrank to 20 nm [15].

Zalite et al., (2015) Cobalt ferrite powders are synthesized by the co-precipitation technology; combined with the hydrothermal synthesis method and crystallite size, magnetic properties of synthesized products are obtained. All the synthesized ferrites are nanocrystalline single-phase materials with crystallite sizes of 10-16 nm and the calculated crystalline size of 20-2 nm. Synthesized Co ferrites are characterized by the saturation magnetization MS of 59-60 emu/g, remanent magnetization Mr of 23 emu/g, and coercivity Hc of 570-650 Oe [16].

Tejabhiram et al., (2016) A facile low-temperature co-precipitation method for synthesizing crystalline cobalt ferrite nanostructures using ferrous sulfate salt as the precursor has been discussed. The prepared samples were compared with nanoparticles prepared by conventional co-precipitation and hydrothermal methods using ferric nitrate as the precursor. Magnetic measurements confirmed the ferromagnetic nature of the cobalt ferrites with low magnetic remanence. Further magnetic hyperthermia studies of nanostructures prepared by low-temperature method showed a rise in temperature to 50 ˚C in 600 s [17].

S.R. Gibben et al., (2017) synthesized of $Ni_{1-x}Co_xFe_2O_4$ (x = 0.3, 0.5, 0.7) by a co-precipitation method using citrate as a chelating agent. The as-prepared powders were calcined at 400, 600, and 800 °C for 3 h in air and characterized by X-ray diffraction (XRD), which confirmed the formation of the ferrite cubic structure of spinel. XRD confirms that the $Ni_{1-x}Co_xFe_2O_4$ nanoparticles belong to a spinel-type network. The linear relationship between particle size and calcination temperatures was observed for $Ni_{1-x}Co_xFe_2O_4$ nanoparticles. $Ni_{1-x}Co_xFe_2O_4$ nanoparticles calcined at 600 °C were characterized using scanning electron microscopy (FE-SEM) techniques [18]

Suresh Sagadevan et al., (2018) synthesized Nickel ferrite ($NiFe_2O_4$) nanoparticles using the co-precipitation method. XRD established the $NiFe_2O_4$ nanoparticles belonging to the cubic spinal structure. The average particle size equals 28 nm. FTIR spectrum also supported the formation of $NiFe_2O_4$ nanoparticles. The nanoparticles agglomerated to form spherical-shaped particles were also confirmed and made clear by the SEM analysis [19].

Muhammad Arshad et al., **(**2019**)** Studied Co-Ni nano-doped co-doped manganese ferrite was synthesized via the co-deposition method. Annealing was performed as nano-ferrite was prepared at 950 °C for 7 h. X-ray powder diffraction (XRD) confirmed that all samples possessed a cubic spinel structure. The size of the crystals was determined by the Scherer equation, which lies in the range of 27-35 nm. Spectroscopy confirmed bond bending and stretching at (B) and tetrahedral (A) octahedral sites. The spectral bands have been shifted towards the longer wavelength side, and these indicate the incorporation of cation dopants (Co-Ni). The magnetic parameters of the MH rings of the ferrite nanoparticles were measured. As the Co-Ni contents increased, the saturation magnetization (Ms) increased up to x = 0.15 and then decreased [20].

Mikio Kishimoto et al., **(**2019**)** Synthesized Co-Ni ferrite spinel particles by chemical co-precipitation and hydrothermal treatment at different temperatures. Microparticles with a few nanometers and spherical or cubic particles with a size of about 30 nanometers, which are responsible for the magnetic properties, were obtained. The crystal size obtained using Scherer's equation was 24-27 nm. The specific composition of the Co-Ni Spinel ferrite particles is expected to influence

the high coercive strength and the observed dependence of the coercive force on the hydrothermal treatment temperature [21].

S. V. Bhandare et al., (2020) Studied changes in spinel ferrites structural and magnetic properties by doping. Magnesium the cation that occupies the tetrahedral position, rather than nickel, occupies. He created nanocrystals at octahedral sites in Co-Ni Ferrite ($Co_{0.5}Ni_{0.5}Fe_2O_4$) ceramics, where he created nanocrystals. Sol-gel $Co_{0.5}Mg_xNi_{0.5-x}Fe_2O_4$ Ceramic Powder Samples (x = 0, 0.1, 0.2, 0.3, 0.4) The spontaneous combustion method was followed by sintering at 600 °C in air for two hours. X-ray diffraction The XRD patterns of the composite samples confirm the single-phase crystalline spinel structure with Cubic symmetry. Crystal sizes were found for all samples.be in the range of 30–38 nm. Scanning electron micrographs FTIR spectra confirm the formation of the spinel phase. Through the observed vibrational bands assigned to tetrahedral (T_d) and octahedral (OH), interstitial complexes in the spinel structure. Magnetic measurements indicate low Saturation magnetization (Ms) with increasing Mg concentration [22].

Sabah M. Ali Ridha et al., **(**2021**)** Studied Preparing nickel-saturated ferrite nanoparticles (NPs) with the chemical formula $Co_{1-x}Ni_xFe_2O_4$ (where, x = 0, 0.5, and 1) using the sol-gel method at low temperature (200 °C). To balance the oxidizing agent, citric acid was used as a chelating agent with a mixture of nickel nitrate and ferric nitrate solutions in a 3:1 ratio .The resulting ferrite NPs were calcined at various temperatures (200, 400, 600, and 800 °C) for 4 h in the air to remove water content and unwanted impurities and to obtain a better structure than the single-phase spinel. X-ray analysis (XRD). XRD analysis shows the structure of a single-phase spinel at the nanoscale. The crystal size calculated from the FWHM of the strongest peak (311) lies in the range

(27-44 nm) for $Co_{1-x}Ni_xFe_2O_4$ ferrite NPs. Because $Co_{0.5}Ni_{0.5}Fe_2O_4$ NPs have a larger crystal size than $NiFe_2O_4$ but smaller than $CoFe_2O_4$ NPs. SEM images show spherical and homogeneous NPs The particle size morphology ranges from 25-47 nm, reflecting the highly crystalline nature of these nanoparticles [23].

Durgadsimi S.U et al., (2021) Synthesized the Nickel ferrite by co-precipitation. X-ray diffraction pattern confirms the formation of cubic spinel structure with lattice constant 8.347Å. Structural properties like X-ray density, average crystalline size, bond length, dislocation density, and microstrain have been studied. The scanning electron microscope images show the grain of bead structures. The Fourier transform infrared spectroscopy spectrum of nickel ferrite under investigation reveals the formation of a cubic spinel structure showing two significant absorption bands, corresponding to high-frequency band $\nu_1$and low-frequency band ν_2 arising from tetrahedral (A) and octahedral (B) interstitial sites respectively [24].

1.3 Aim of the Present Work

1. preparation Co-Ni ferrite nano particles by simple and very fast methods.
2. Studying the structural properties of XRD,FTIR,FE-SEM and the magnetic properties VSM of the prepared particles
3. Improving the properties of the prepared nickel cobalt using pulsed laser deposition
4. Testing the effectiveness of nano-ferrite as anti-bacterials against two types of Gram-positive and Gram-negative bacteria

Chapter Two

Theoretical Part

2.1 Introduction

Nano-sized Due to a special property known the phenomenon of super para magnetism , magnetic materials have unique magnetic properties. Magnetic nanoparticles are important for biological applications because of their small size in comparison to biological entities as well as their unique magnetic properties. [25]. Many biological applications, such as magnetic resonance imaging, have made use of magnetic nanoparticles (MRI). [26] hyperthermia treatments [27], drug delivery [28], tissue engineering and bio-analysis [29].

2.2 Ferrite

"Ferrites" are ferromagnetic materials that resemble ceramics that are mostly made of ferric oxide, Fe_2O_3 [30]. Ferrites have various advantages over ferromagnetic alloys, such as improved corrosion resistance, greater heat resistance, and lower cost, because their saturation magnetization is significantly lower than that of ferromagnetic alloys, by as much as a factor of two. By fully using these benefits, several practical uses of ferrites have been expanded [31].

Magnetite, (Fe_2O_4) which is a natural mineral, a genuine ferrite, and it is said that ancient people had recognized its magnetism and that it was used as a mariner's compass in China more than two millennia ago. The first attempt to prepare various types of ferrites and to industrialize ferrites was not made until the beginning of this century. Rapidly development of radio, television, carrier telephony, and computer circuitry and microwave devices arouse attention of people to the importance of these ferrite materials. Since then the science evidenced the tremendous advancement in the field of manufacturing and processing of ferrite materials. [31,32] Spinel, garnet, and hexagonal

ferrite are the three most common forms of ferrites, based on their crystal structure and constructions [32].

2.3 Spinel ferrites (Cubic ferrites)

Spinel is the most widely used family of ferrites. They are also called cubic ferrites. High values of electrical resistivity and low eddy current losses make them ideal for their use at microwave frequencies.

The term spinel comes from the Italian word spinel, which means thorns in English (from the pointy crystals that make up its structure). Spinel crystallizes in the cubic system as octahedral crystals. A spinel supergroup contains at least 30 oxide minerals. The space group Fd_3m contains the bulk of spinel chemicals. Magnesium, iron, nickel, manganese, and zinc are examples of divalent metals that make up the most abundant ion in the group therefore, its chemical formula is AB_2O_4. This position can also be occupied by the Tetravalent lead ion. The letter "B" stands for trivalent metal ions, such as copper and zinc [33].

The chemical formula for spinel ferrite is MFe_2O_4, where M is any divalent metal ion with an ionic radius of 0.6 to 1. Manganese (Mn), iron (Fe), cobalt (Co), nickel (Ni), copper (Cu), zinc (Zn), and magnesium are all metals, and there are several transition elements between them (Mg). and Cd in simple ferrites.

A combination of these ions is also possible, a mixed ferrite. The symbol M can represent a combination of ions which have an average valency of two e.g. Li^{1+} and Fe^{3+} in lithium ferrite, $Li_{0.5}Fe_{2.5}O_4$. The trivalent iron ions (Fe^{3+}) in MFe_2O_4 can be completely or partly replaced by another trivalent ion such as Al^{3+} or Cr^{3+}, giving rise to mixed crystals with aluminates and chromites. The spinel lattice is composed of a close-

packed oxygen arrangement in which 32 oxygen ions form the unit cell (the smallest repeating unit in the crystal network). These anions are packed in a face centered cubic (FCC) arrangement leaving two kinds of spaces between anions: tetrahedral coordinated sites (A), surrounded by four nearest oxygen atoms, and octahedral coordinated sites (B), surrounded by six nearest neighbor oxygen atoms. In total, there are 64 tetrahedral sites and 32 octahedral sites in unit cell, of which only 8 tetrahedral sites and 16 octahedral sites are occupied, resulting in a structure that is electrically neutral [34,35]. Spinel is classified on the basis of the distribution of cations into three types:

2.3.1 Normal spinel

In the case of the normal spinel, the divalent ions are all on A sites and trivalent ions occupy B sites. In the elementary unit cell of spinel structure eight tetrahedral and sixteen octahedral sites are occupied by metal ions. This can be represented by the formula $[M]^{tet}$ $[Fe]^{oct}$ O_4. where, M divalent ion and Fe trivalent ion [35]. Examples of normal spinel are ,$FeO.Al_2O_3 = FeAl_2O_4$,$CoO.Al_2O_3 = CoAl_2O_4$.

2.3.2 Inverse spinel

In the inverse spinel, the divalent ions occupy only B sites while trivalent ions are located on both A and B sites in equal proportion. The inverse spinel, B (AB) O_4, has the divalent cations occupying the O-sites and the trivalent cations are equally divided among the T- and remaining O-sites. This can be represented by formula, $[B]^{tet}$ $[A, B]^{oct}$ O_4. $CoFe_2O_4$ is predominantly an inverse spinel with a formula; Co_xFe_{1-x} $(Co_{1-x}Fe_{1+x})$ O_4 (with x 0) where x is the cation distribution factor which describes the fraction of tetrahedral sites occupied by Co^{2+} cations [35]. Examples of inverse spinel are Co O $Fe_2O_3 = FeCoFeO_4$, $NiO.Fe_2O_3 = FeNiFeO_4$.

2.3.3 Random spinel

It has an intermediate cation distribution, these are the ferrites having ionic distribution between normal and inverse spinel ferrites are known as mixed ferrites, represented as $[B_{0.67}\ A_{0.33}]^{tet}\ [A_{0.67}\ B_{1.33}]^{oct}O_4$. Like Ni-Zn ferrite. The variable γ is the inversion parameter, which specifies the fraction of A-sites occupied by majority ions.

levels are normal $[A]^{tet}$, $[B]^{oct}\ O_4$. γ=0

The formula is $[B]^{tet}$, $[A, B]^{oct}\ O_4$ invert. γ=1

$[B_{0.67}A_{0.33}]^{tet}\ [A_{0.67}B_{1.33}]^{oct}\ O_4$ Random γ=0.67

The inversion parameter is a measure of the degree of inversion and in some ferrites depends on the method of preparation. [36].

2.4 Cobalt Nickle Ferrite Structure (Co-Ni FS)

Both $CoFe_2O_4$ and $NiFe_2O_4$ crystallize into a spinel-type structure, represented by the formulas $(Fe^{3+})\ [Co^{2+}Fe^{3+}]O_4$ and $(Fe^{3+})[Ni^{2+}Fe^{3+}]O_4$, respectively. Tetrahedral (A) sites are occupied by cations denoted by round brackets, whereas those in square brackets occupy octahedral (B) sites in the structural formula shown. The technique of production, chemical composition, and sintering temperature all play a role in how the cations are distributed inside the crystal lattice.

The characteristics of ferrites are altered depending on how the cations are distributed between the tetrahedral and octahedral sites. The total magnetization of ($CoFe_2O_4$) and ($NiFe_2O_4$) is equal to the difference between the magnetizations of sublattices (A) and (B).

Due to their mutually cancelling magnetic contributions, (Fe^{3+}) cations at (A) sites and (B) sites Only unpaired spins of the (Co^{2+}) and

(Ni^{2+}) cations control the net magnetization of mixed ferrites like $Co_xNi_{1-x}Fe_2O_4$. Co^{2+} ions have three unpaired spins, while Ni^{2+} ions only have two. Mixed ferrite $CoxNi_{1-x}Fe_2O_4$ is formed when Co^{2+} is incorporated into $NiFe_2O_4$, resulting in a little modification to the cell parameter of the cubic spinel $NiFe_2O_4$. However, when cobalt (Co) is added to $NiFe_2O_4$, the following values increase:

(1) the anisotropy of magnetization in crystals (and consequently the magnetization)

(2) Because of its high coercivity (Hc), it has promising future uses in magnetic recording (MR) (37).

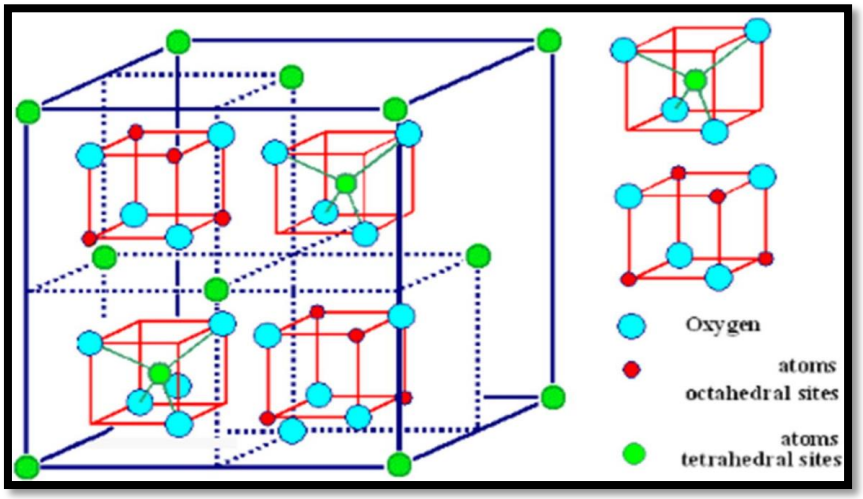

Figure (2.1): Unit cell of spinel structure $MeFe_2O_4$ [37].

2.5 Magnetic metal oxide nanoparticles

Mixed and metallic oxide nanoparticles indicate unique properties such as great magnetic properties, high surface area, high adsorption capacity, and high chemical stability, thereby attracting great attention in various fields. Among these nanostructures, some of them such as spinel ferrites, Fe_3O_4, TiO_2, Al_2O_3, ZrO_2, MnO, and CeO_2, both in bare form or modified with different functional coatings, are of particular interest [38].

investigated magnetic nanoparticles extensively and magnetic metal oxide nanoparticles (MMONPs) in particular. These are oxides that consist of two different structural oxidation states:

(1) The presence of cationic states with varying valence

(2)Deficits in anion levels (vacancies) [39].

These MMONPs are part of a larger group of smart and valuable materials that show properties including semi- and superconductivity, and magnetic properties. [40].

There are numerous of different metal groups, and each has its own unique structure and properties that make up MMONPs. Metal oxides (including iron and nickel oxides, and even lanthanum strontium manganite) and ferrites make up the bulk of these NPs. It is possible to generate heat using magnets [41], and this ability makes iron oxides a potentially useful tool in the field of hyperthermia therapy.

Oxides (Fe_3O_4, -Fe_2O_3, hematite, iron oxide beta phase) are the most common, followed by oxyhydroxides (feroxyhyte, akaganeite, goethite, and lepidocrocite), and then hydroxides (iron (II) hydroxide, and iron (III) hydroxide). [42]. In addition to iron oxides, ferrites typically contain at least one metal with desirable magnetic and dielectric properties.

M (Fe_xO_y) is a formula for ferrites, in which M stands for x and y can be anything, and M and Cu and Al and Bar and Ni and Co and Fe are all acceptable values for the metal cation x. [43]. Due to their versatility, ferrites are widely used in a variety of applications, including sensors,

MRI, biological imaging, catalysts, and electromagnetic and optical devices [44].

A huge amount of MMONP NPs' size and shape should be modified for each application. consistently aligned. Hence, the accomplishment of these goals is dependent on monodispersed NPs. As a result, MMONPs have been synthesized using a variety of techniques Methods such as ball milling and co-precipitation (or hydrothermal) or sol-gel (or micro emulsion) are among the mechanical approaches mentioned in [45]. However,it was found out that the synthesized MMONPs were partially improper for the above-mentioned applications, with difficulties Aggregation, hydrolysis, condensation, and dimensional heterogeneity are all examples.

2.6 Types of Magnetic Materials

The magnetic properties of most substances can be categorized as diamagnetic, paramagnetic, or ferromagnetic. figure (2.2) showing different kinds of magnetic materials

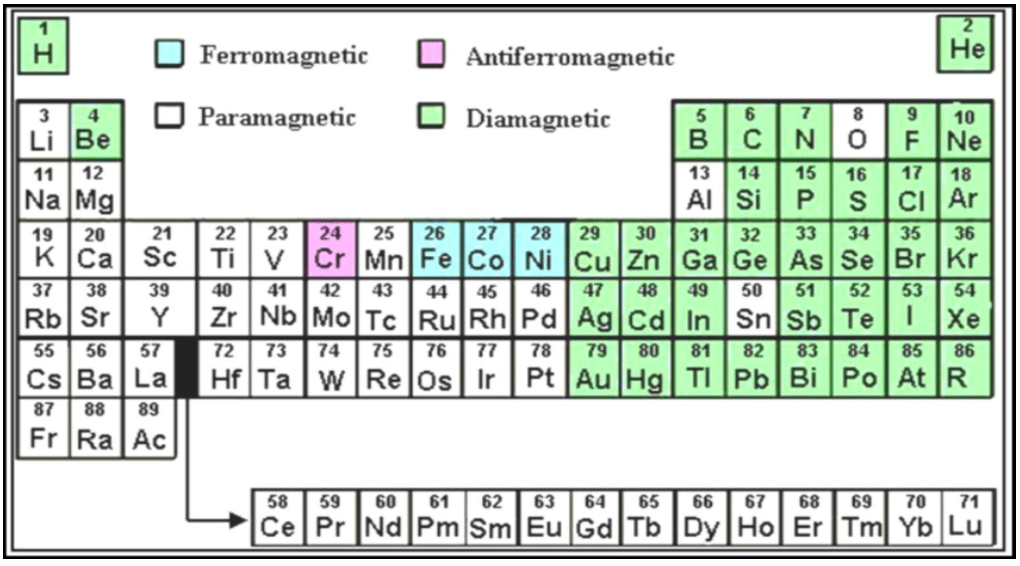

Figure (2.2): Periodic table showing different kinds of magnetic materials[46]

2.6.1 Diamagnetism

Diamagnetism in a material arises when there are no unpaired electrons . When this happens, the net magnetic moment of a material is zero, until forced into orientation by the application of an external magnetic field. The magnetic moments oppose the applied magnetic field, creating a very small, negative, unchanging susceptibility. Superconductors are also perfect diamagnets when they are in their superconducting state [46].

2.6.2 Paramagnetic

Para magnetism in materials arises when unpaired electrons do exist in that material[47]. The magnetic moments in a paramagnetic material are initially randomized, but will tend toward the direction of an external magnetic field. Para magnetism differs from diamagnetism is that the susceptibility created by this class of materials is positive and unchanging. Hence, the magnetic moments that align in the same direction as the magnetic field are weakly interacting. This also implies that when the external magnetic field is removed, the magnetization returns to zero. Paramagnetic and diamagnetic materials are often considered non-magnetic. [47]

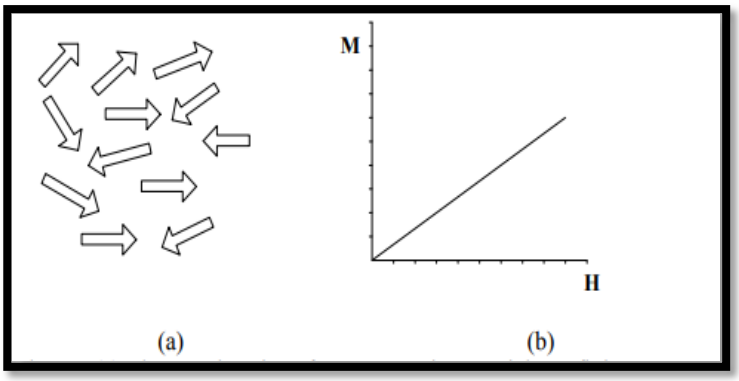

Figure (2.3): (a) The atomic spins of paramagnetic material at a finite temperature, (b) Magnetization change as a function of magnetic field [47].

2.6.3 Ferromagnetism

Ferromagnetism in materials arises when unpaired electrons exist and strong interactions between magnetic moments are present [48]. These strong interactions occur below a characteristic temperature , at which a phase transition takes place from a paramagnetic to a ferromagnetic state[46].

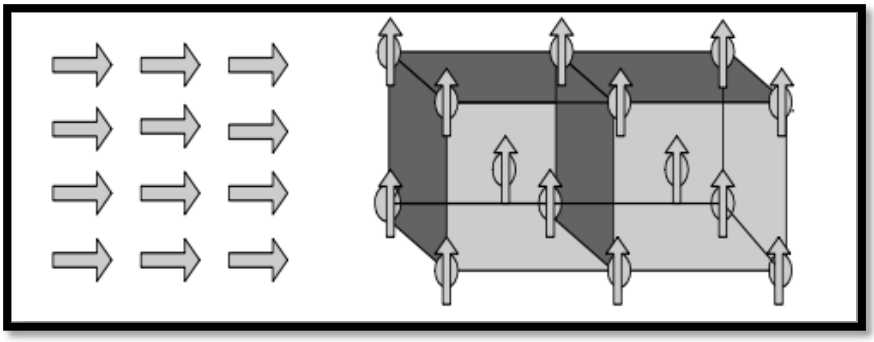

Figure (2.4): Parallel alignment of spins in ferromagnetic materials [47].

2.6.4 Antiferromagnetism

Antiferromagnetism arises when the nearest neighbor magnetic moments in a material point in opposite directions [49]. This pattern of magnetic moments arises from two separate sublattices of magnetic moments that are separately ordered ferromagnetically, but in opposite directions. in the absence of an external magnetic field, antiferromagnetic materials have no net magnetization. Analogous to the Curie temperature of ferromagnets, there exists a transition temperature with antiferromagnets called the Néel Temperature, above which the sample displays paramagnetism. If an external magnetic field is strong enough, the magnetic moments in the oppositely oriented sublattice will conform to the first one, and all magnetic moments in the material will be aligned, thus saturating the sample. [50].

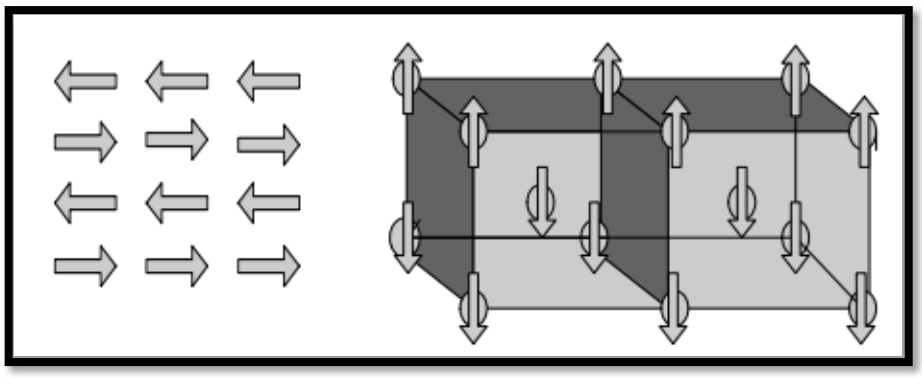

Figure (2.5): Antiparallel arrangement of spins in antiferromagnetic lattice [47].

2.6.5 Ferrimagnetism

Ferrimagnetism shares some similarities with ferromagnetism and antiferromagnetism [51]. Like with antiferromagnetism, ferrimagnetism arises from the formation of two oppositely aligned magnetic sublattices. However the sublattices have different magnitudes for their magnetic moments leading to an overall magnetization in one direction, much like ferromagnetism, Because of this, the sample appears to behave much like a ferromagnet. Many materials that display ferrimagnetism have spinel or inverse spinel crystalline structures, meaning that they are of the form AB_2O_4. Materials discussed in this thesis are of the inverse spinel structure, such as cobalt ferrite ($CoFe_2O_4$) and magnetite (Fe_3O_4, $Fe^{2+}Fe^{3+}{}_2O^{2-}{}_4$)[52].

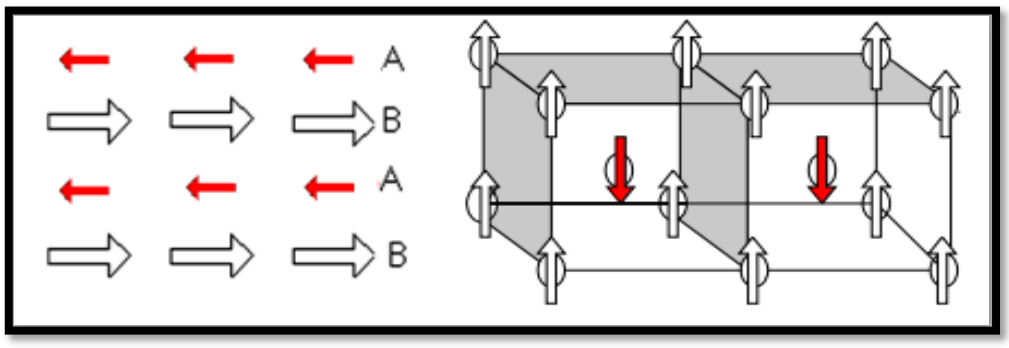

Figure (2.6): Spin arrangement of ferrimagnetic crystal, A and B are the tetrahedral and octahedral sites respectively[47].

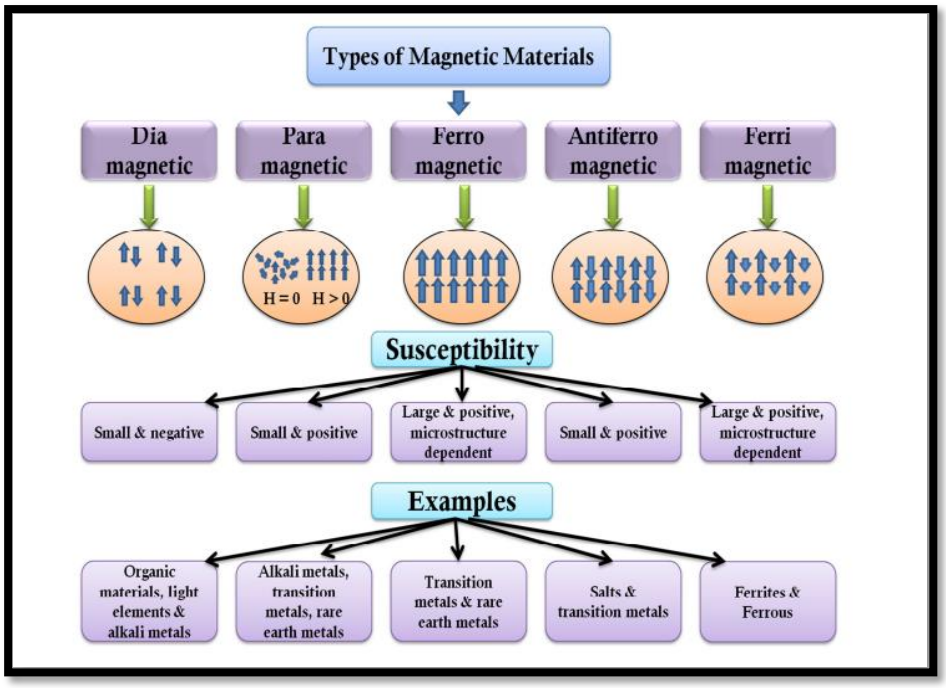

Figure (2.7): Flow chart of different types of magnetic materials [48].

2.7 Hysteresis loop and magnetic parameters

By analyzing the hysteresis loop, can be learned a great deal about the magnetic materials. The magnetization state of a material is a function of the strength and direction of the magnetizing field. Let we consider many small magnetic domains in a specific material, but there is no net magnetization, we can test what happens to the domains as the field strength is increased [53].

Figure 2.8 schematically illustrates a hysteresis loop (magnetization M as a function of an applied magnetic field H). Hence, a hysteresis loop is obtained by measuring the magnetic moment of a sample, where the applied field is cycled between the broad limit of positive and negative values [54].

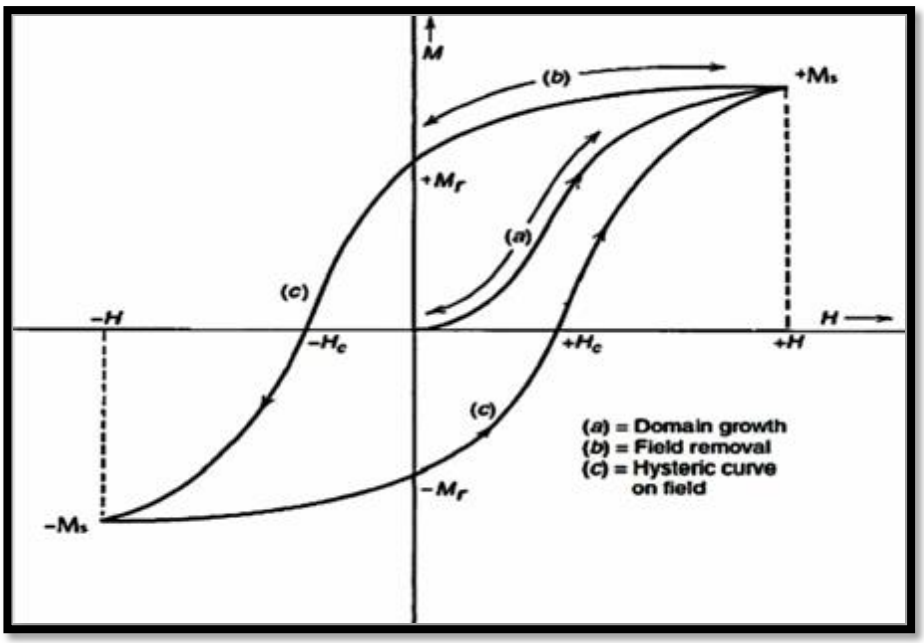

Figure (2.8): Hysteresis loop for ferromagnetic materials [55].

A magnetic induction, M, occurs when an unmagnetized material, such as iron, is put using magnetism, H. When the magnetic The field is raised, as indicated in curve (a) of figure 2.8, the magnetic induction increases.

The domain growth region is the name given to this area. The magnetization approaches its saturation point at sufficiently high applied fields when all magnetic dipoles are aligned with the external field. The saturation magnetization (MS) is the greatest value of magnetization reached in this condition; at this point, the magnetization becomes constant. [55,56].

When the magnetic field is back to zero, spins cease to be aligned with the magnetic field, result, decreases in the total magnetization. The magnetization with respect to the field curve does not follow the path of the initial curve but instead lags behind, as shown in curve (b), results in a permanent induction, called the remnant induction (remanent

magnetization M_r).[53,57], Even when the applied field is zero, the material remains magnetic. Since the domain wall motion is constrained and the domain creation process is not fully reversible, the spin orientations within domains have not yet rotated back to their favourable crystallographic locations, but this is not a problem. [55].

As illustrated in curve (c), to return the induction of magnetism equal to zero, an antiparallel magnitude field (H_C), known as It is imperative that the coerciveness be made available to initial The magnetic field, as illustrated in curve (c). An increase in the strength of the magnetic field in the opposite direction causes magnetic saturation (M_S) in that direction. Along with enduring worths (M_r). When the field is turned around again, the loop's Induction in a Field closedThe area inside the hysteresis loop is proportional to the amount of energy dissipated during one cycle as a function of the material's volume. [55].

By reversing the direction of the applied field, the hysteresis loop is broken. The amount of effort needed to alter the configuration of magnetic domains. is represented by the hysteresis loop area, whereas the product M-H, also known as the energy product, reflects the net loss in the system, which is generally in the form of heat [53].

2.8 Methods of Preparation for Nanoparticles

Ferrites are like other ceramic materials, and to prepare them requires first identifying the raw materials that may be in the form of oxides or salts of elements such as carbonates, chlorides or nitrates and determining their weights accurately, then comes the mixing stage, which aims to obtain a 99% homogeneous mixture to prevent any agglomeration of materials or collected in a specific site, and there are many ways to prepare nanomaterials, the most important of which are:

(a) The technique of chemical co-precipitation.

(b) Sol - Gel method [58].

In this study, we will focus be on the normal co-precipitation method combined because it is the method that was adopted to prepare magnetic nanoparticles. Depending on the type of anchoring material, this technique employs one of two chemical deposition processes, the most essential of which are:

2.8.1.Hydroxides Precipitation

This method is done by adding an alkaline base such as sodium hydroxide, NaOH, or ammonia to solutions containing metal ions in the composition of the spinal ferrite, such as metal chlorides, oxides, sulfur, or carbon, and there are parameters through which you can control the pH that must range between(8-12). In a solution of hydroxides, the metals begin to precipitate depending on the pH value, which has a very large effect on the shape of the sedimentary particles as well as on their size.

The oxidation process is carried out with or without aeration. After the precipitate is obtained, the filtration phase begins using filter paper or using a centrifugal center fug. After that, the residual mixture is washed with water or alcohol several times in order to get rid of the remnants of the precipitate until the acidity is equalized (PH= 7). After that, the resulting powder is dried at a suitable temperature to get rid of ordinary water and the rest of the carbonates.

The pH value is one of the most important factors by which the sedimentation speed is controlled, as well as determining the value of hydroxides that have constant solubility in solution. Some researchers have used this method to prepare ferrite manganese-zinc. One of the most

important advantages of this method is that it gives greater homogeneity to the mixture, which helps to reduce the temperature, so the powders do not need high temperatures during the sintering process either.

As a method that shortens the long grinding periods to obtain magnetic powder and the possibility of producing thin films in this way, despite the advantages of this method, it is considered one of the methods that may not give pure and accurate phases if the reactants have different solubility and sedimentation rates. [59]

2.9. Pulsed Laser Deposition (PLD)

The technique of ablating a material with laser had become an important subject in the past years because it's simple, fast, cheap, and pure nanoparticles thin films and capable to grow high-quality thin films at low temperatures [60]. The nanoparticles growth process can be controlled easily by manipulating the physical parameters of PLD process, like laser energy, frequency, fluence, wavelength, number of pulses, background pressure and gas medium and distance between target and substrate [61].

The disadvantage of this technology, on the other hand, A major drawback, however, [62] is that only very targeted areas may be deposited upon. Nanoparticles of many different materials, including semiconductors, metals, ferroelectrics, dielectrics, organics, composites, polymers, ceramics, metal oxides, etc., can be synthesized using PLD. [63].

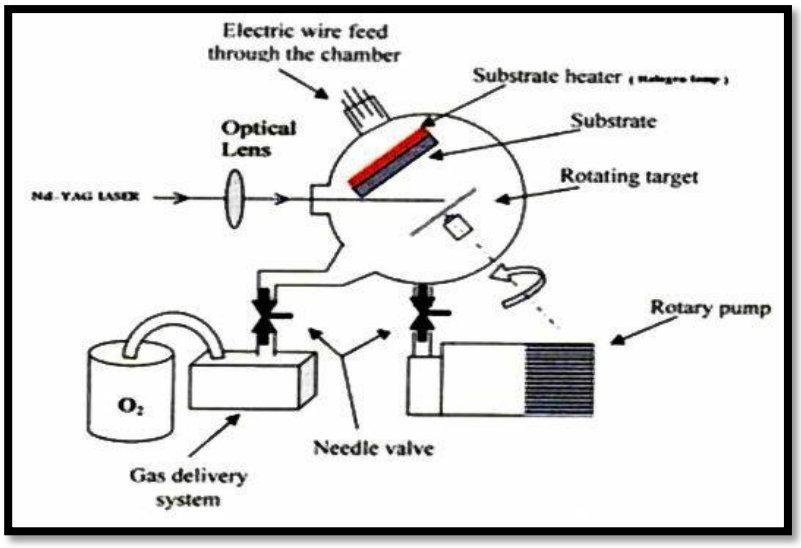

Figure (2.9) demonstrates a schematic diagram of the PLD technique (60,61).

The process of PLD is basically starter with high energy laser beam pulse focused on a solid target surface, which penetrates in a certain depth the material's surface depending on the material refraction index and the laser wavelength. The laser beam is sufficient to produce a strong electric field that removes electrons from the penetration area in a time shorter than the laser pulse duration.

The freed electrons move in the produced electromagnetic field and collide with the bulk material's atoms, giving some of its energy to the bulk lattice, which causes the target surface to heat up and vaporizes. The material vapor is converted to plasma at enough high laser energies that contain many energized species like molecules, atoms, ions, electrons, molten globules, and clusters.

Induced plasma is very pressurized, dense, and hot. This results in a significant pressure differential when compared to the surrounding air. The plasma plume expands quickly and cools due to the pressure gradient. Then, at the right pressure and temperature, the plasma species

will nucleate and develop into nanoparticles on the depositing substrate [64].

2.10. Thermal coefficients

Increasing the ductility and hardness of steel by adjusting the heating temperature and dwell time is one use of thermal coefficients. It is a set of methods used to improve the material's physical and, in certain cases, chemical qualities. The most important of these processes is calcination. It is a heat treatment process that is applied to powders and solid materials in order to cause thermal decomposition or a phase transformation, as well as remove the volatile parts of unwanted materials.

The calcination process usually takes place at a temperature below the melting point of the substance. Oxalates, sulfates, nitrates, carbon, and some alkaline oxides (NO_3, H_2O, CO_2, SO_4) are volatilized by heat during the calcination process [65] .

2.11. Pressing Process

After the heat treatment stage, the powder is well milled to obtain the required ferrite powder. Individual or ring-shaped samples are created by squeezing the powder via a specialized piston, and they are then studied and analyzed. The mechanical properties of pressed powders are weak and may turn back into powder due to the effect of force.

Weak mechanical In order to give the manufactured material the necessary physical and chemical properties, the sintering process takes place on the materials where changes occur during the heat treatment processes In the microscopic structure, such as an increase in grain size,

as well as a change in the shape of the pores and a decrease in the size of the porosity, Figure (2.10) is pumped into the powder bag mechanism [66].

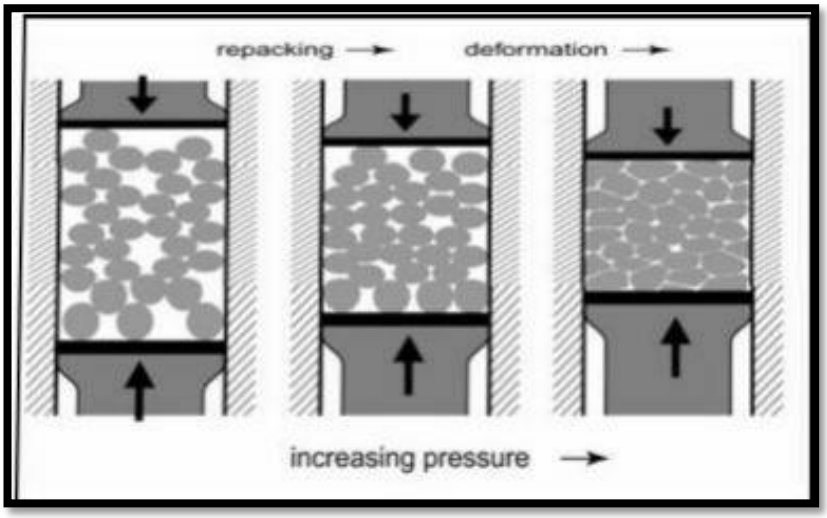

Figure (2.10): shows the powder compaction mechanism [66].

2.12. Sintering

Sintering is a heat treatment method used to obtain powder products by burning the material at temperature lower than its melting point, where the atoms of the material in the form of powder adhere to each other.The process leads to an increase in the crystalline size of the material due to heat. These processes occur The most important ones are:

1. As a result of heat transmission from the horn to the surface of the reactant.
2. Reaction at the reactant's surface
3. The occurrence of diffusion of the gas produced from the reaction surface through the layers of oxides generated in the atmosphere of the furnace.

These processes are often endothermic, as the amount of this heat depends on the amount of free energy for the dissolution of salts, oxides, and volatile gases. The presence of a mixture of carbonates and oxides in this process leads to a partial interaction between the oxides produced in the mixture, and the amount of this reaction depends on the temperature and the effectiveness of the components. basic mixture [67].

2.13. Bacterial Types

Research microorganisms are often classified as either positive or negative Gram stain groups [68–69]:

2.13.1.Escherichia coli (Gram (ve-))

rod (bacillus) in the family Enterobacteriaceae. Most *E. coli* are normal commensals found in the intestinal tract. Pathogenic strains of this organism are distinguished from normal flora by their possession of virulence factors such as exotoxins. Bacteria generally exist in the intestines of healthy people and animals. Most of its types are harmful or cause relatively brief diarrhea. As well as Escherichia Coli caused contamination of water or food [70].

2.13.2.Staphylococcus bacteria (Gram (ve+)):

This type of bacteria is normal flora a skin or in the nose of healthy people. It is typically caused no disease. This group of bacteria that cause a multitude of diseases. Under a microscope staphylococcus bacteria are round and bunched together. They can cause illness directly by infection or indirectly through products, they make, such as the toxins responsible for food poisoning and toxic shock[71].

2.14 Antibacterial Activity of Nanoparticles

Antibacterial agents inhibit the growth of a big range of microbes such as bacteria, fungi, and viruses [72]. Antibacterial synthetic like plant or chemically modulated natural compounds [73]. When materials are synthesized in the form of very small particles their physical and chemical properties will change. This variation in the properties is resulting from the fact that in nanoscale dimensions' percentage of surface to volume comparing to bulk molecule is high [74].

Nanotechnology includes the materials at the atomic level to obtain special properties which has been required for certain applications. Therefore, a concourse of nanotechnology and biology can resolve many biomedical problems and make a revolution in the field of health and medicine [75]. Nano biotechnology is a big expression together biotechnology and Nano technology. Nano biotechnology can mean building tiny tools to change natural structures atom by atom and using it for various biomedical applications [76].

Antibacterial agents are classified into two types: the organic and inorganic classes. The organic antibacterial materials have been used as bactericides for several years. Because of high temperatures in the manufacturing procedure their antibacterial properties will be reduced so they have some damage involving toxicity to the in – vivo. The attention in inorganic bactericides like metal oxide NPs is growing [77] as a result of their thermal stability improved safety and excellent resistance against bacteria [87]

Development of bacterial strains resistant to some pharmaceutical has become a serious health dilemma the emergency to improve new bactericidal materials is raised. Realizations have present hopeful

consequence about action of various treatment and antibacterial formulation in the form of NPs [79].

Advances in nanotechnology have led to the production of nanosize organic and inorganic molecules with possibility applications in textiles industry, medicine food packaging and the rape tics. The development of the new nanoparticles antibacterial agent Nano composites can be used as an alternative planning to overcome antibacterial resistance [80]. Nanomaterial can be used in therapy containing targeted drug delivery the detection of tumors (cancer) and prediction optical monitoring of therapy [81 -82].

2.15 Structure properties of ferrite

X-ray diffraction is an adaptable, non-destructive method of gaining insight into materials. A crystal lattice consists of atoms that are consistently distributed over three spatial dimensions (cubic, rhombic, etc.). In its design, they create a set of parallel planes that are separated by a distance d (inter-planar or inter-atomic distance) that varies depending on the substance. There are many possible plane orientations in a crystal, and each has its own unique d-spacing [83].

X-rays are electromagnetic radiations having wavelength in the range of 0.5 to 2.5Å. This wavelength of X-rays is comparable to the interatomic spacing in solids [84]. Radiations of longer wavelength cannot resolve the structure on an atomic scale and radiations of much smaller wavelength are diffracted incontinently through small angles. X-rays can be produced either by the deceleration of fast moving electrons in the metal target or by the inelastic excitation of the core electrons in the atoms of target. The first process gives broad continuous spectrum while second gives the characteristic X-rays [85].

The typical X-ray diffractometers consist of three main parts such X-ray source, a sample holder, and X-ray detector. The sample holder is in the middle of a circular with the source and detector and their accompanying optics around its periphery. Bragg‟s law is the basis of XRD analysis. The angle between the plane of the sample and the X-ray source is (θ), known as Bragg‟s angle, When an X-ray is projected onto a detector, the angle between the projection and the detector is (2 θ). Figure (2.11), in which the diffraction angle 2 is the angle between the incident and diffracted Xrays [86], depicts the fundamental components of an X-ray diffractometer.

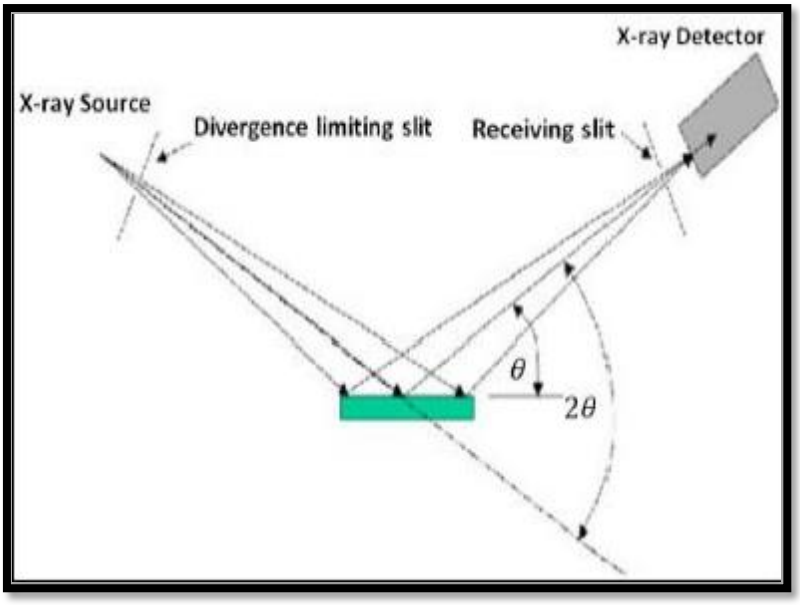

Figure (2.11): Schematic representation of x-ray diffraction [86].

All crystalline substances have their own distinctive atomic structure, which causes them to diffract X-rays in their own special way. Figure (2.12) shows the Bragg‟s diffraction from parallel planes.

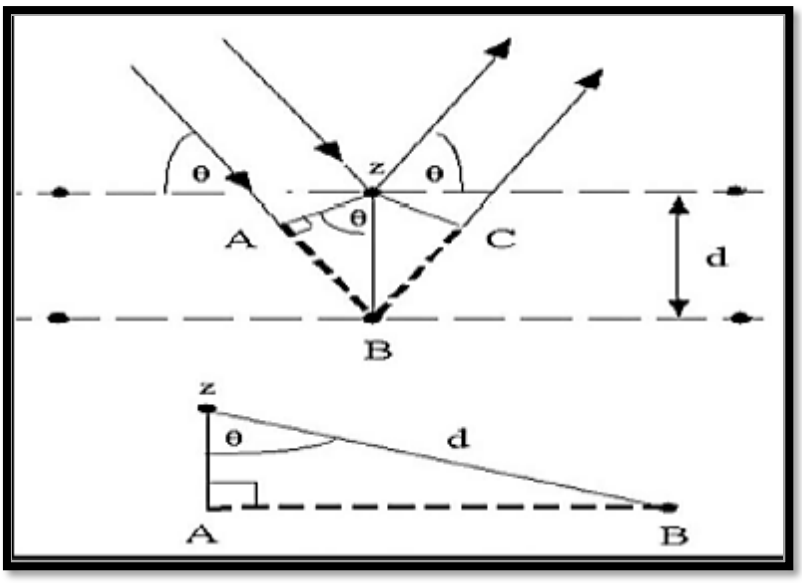

Figure (2.12): Constructive interference from the parallel planes [86].

In order to observe the diffraction phenomena, it is necessary to satisfy the geometric condition that the wavelengths of the incident X-rays be on the same order as the distances between the atoms in the crystal If the crystal plane is aligned in accordance with Bragg's law, then an incoming X-ray beam will be diffracted. The formula for Bragg's law is [87]:

$n\lambda=2d \sin\theta$……..(2.1)

The distance between atomic planes, d, the half-value of the diffraction angle, and the reflection order, n, are all factored into the equation for X-ray diffraction, where. A detector's scanning of the range angles of a reflection yields a pattern of peaks with distinct intensities and spacing [88]. Spinel crystals form in the cubic system in spinel ferrite [89]. For the cubic lattice, we get the following equation for the lattice constant (a):

$a_{exp} = d_{hkl}\sqrt{h^2 + k^2 + l^2}$ ……..(2.2)

Where, (hkl) Miller indices, (d_{hkl}) interplanar distance, h, k, and l . In addition, x-ray density (x) ,it influenced by the crystal's molecular weight and lattice parameter, and is given by the following equation:

$$\rho_x=\frac{Z\,M}{N_A\,V} \quad \text{..... (2.3)}$$

The number of molecules in unit cell is denoted by Z (Z = 8 for spinel ferrite), the sample's molecular mass expressed by M, the cubic structure's volume is $V=a^3{}_{exp}$, Avogadro's number is $N_A= 6.023 \times 10^{23}$ (atom/mole) [90]. According to Scherrer's equation, the crystallite size was estimated from the peak broadening on XRD pattern [91]:

$$D=\frac{K\,\lambda}{\beta\,cos\theta} \quad \text{.....(2.4)}$$

Here, D is the crystallite size, λ is the X-ray wavelength, θ is the diffraction angle, is the finite size broadening, and K is the form factor (K =0.94) for spherical crystallites with cubic symmetry [92].

The variation of distance between magnetic ions in the tetrahedral A-site (L_A) and the distance between magnetic ions in the octahedral B-site (L_B) using the relations:

$$L_A = \frac{\sqrt{3}a}{4} \quad \text{..... (2.5)}$$

$$L_B = \frac{\sqrt{3}a}{2} \quad \text{..... (2.6)}$$

2.16 Fourier transform infrared spectroscopy FTIR

The infrared spectroscopy examinations within the range (400-4000) cm^{-1}at room temperature using an infrared spectrometer FTIR give us information about the vibration of the lattice and the crystal structure, and how the ions are distributed between the tetrahedral and octahedral sites and thus the mechanical properties are determined by determining The force constant for the two sites B: KB, A: KA also gives us information about the structure type of ferrite spools, and Figure (2-13) shows an illustrative diagram of the work of the FTIR device [93]

Figure (2-13): schematic diagram of the operation of the FTIR device [93].

2.17 Field Emission - Scanning Electron Microscopes(FE-SEM)

FE-SEM analysis is one of the microscopic techniques a technique developed by the scientist Erwin Muller to reveal more about the surface's shape or composition. Nanotechnology has strongly pushed the development of the modern electron microscope, not only to obtain an accurate increase in measurement but also to obtain more structural information for the sample.

The FE-SEM (field-emission scanning electron microscope) is a powerful technique for developing surface morphology by point scanning, using a high-energy beam of electrons and a high resolution of up to a few nanometers when an electron beam is shed using electrostatic lenses on a very narrow focal point. Or magnetic and electrostatic lenses are usually used for this purpose by scanning the microbeam on the surface of the sample using a scanning generator where the electrons interact with the atoms constituting the material (the sample) to produce signals.

The signals thus obtained transmit information about formation or surface formation and other these signals include secondary electrons, scattered electrons, phonons, light, and temperature, and thus these signals are commonly used for imaging samples, where the secondary electrons are thought to be the most valuable for demonstrating modulation on the samples and the scattered electrons are thought to be the most important for clarifying data on the multiphase structure of the samples [94].

Figure (2.14): FE-SEM analysis.[94]

2.18 Magnetic Measurements Techniques

2.18.1 Vibrating Sample Magnetometer (VSM)

Researching materials' magnetic characteristics relies heavily on this method. This technique was developed by the researcher, Former, so sometimes it is known as the Former Magnetometer.

This technique depends on calculating the shift in the magnetic flux from a coil when the model with magnetic property is allowed to vibrate or vibrate near it. in the form of a small annular disk attached to the end of a rod of a non-magnetic polymeric material called "Taqlon". Figure (2.15) shows the technique of measuring magnetic properties VSM [95].

Figure (2.15): shows a simplified form of the VSM technology [95].

The emergence of this vibrational movement leads to the emergence of a vibrating electromotive force A.C in the coil, which is a relative value of the magnetic moments of the model to be examined. The material's hysteresis ring, which can be transformed in terms of the magnetic moment m, magnetization of the material M, or magnetic flux intensity B, and the motor that generates the vibration must vibrate with a

range that does not exceed 40 Hz and an oscillation distance that does not exceed (2-3 mm), and the sample's weight does not exceed (1g).

VSM technology is an effective and highly sensitive technique for materials that have both strong and weak magnetic properties. It is also possible to conduct VSM tests for materials at high and low temperatures. The saturation magnetization Ms is calculated using the deceleration loop. The hysteresis Mr. and compulsive domain Hc values [96].

Chapter Three

Experimental Work

3.1 Introduction

This chapter describes the equipment and materials used to synthesize the Co-Ni ferrite nanoparticles as a powder by the co-precipitation method .Structure and magnetic properties were tested using XRD, FE-SEM, FTIR, and finally, the Vibrating Sample Magnetometer (VSM). Co-Ni ferrite nanoparticles convert to pellet and irradiation by laser Nd: YAG of wavelength (1064nm) to enhance the properties of samples. Analyze the impact of Co-Ni ferrite nanoparticles on several bacterial species.

3.2 Materials

This study uses iron nitrate, nickel nitrate, cobalt nitrate, Sodium hydroxide and distilled water. The compounds were purchased from sigma aldrich Company and imported from Germany. The physical and chemical properties for materials are shown in table 3-1. The molar mass of every material is calculated from its atomic weights. Two moles of iron nitrate, one mole of nitrate (cobalt and Nikel), and one mole of fuel are added to the combination of ferrite series following the accepted proportion stoichiometric weight.

Table (3-1) Chemicals Used.

Compounds	Chemical formula	Mol.Mass ($g.mol^{-1}$)	Purity %	Supplier
Iron nitrate	$Fe(NO_3)_3.9H_2O$	403.8	99	Fluka
Cobalt nitrate	$Co(NO_3)_2.6H_2O$	291.031	≥ 97	BDH
nickel nitrate	$Ni(NO_3)_2.6H_2O$	290.79	99	BDH
Sodium hydroxide	NaOH	40.00	98	Alpha Chemicals

3.3 Tools and equipment

3.3.1 Mass Measurement Instrument

Was employed in this research. A balance with four decimal places and a high degree of sensitivity.

3.3.2. Magnetic Stirrer

It is a lab instrument that rapidly spins a stir bar dipped in a liquid to stir it. The magnetic field used in the tool rotates. To create a consistent mixing environment for the atoms and liquid particles, magnetic stirrers typically feature a heated plate or other ways of heating the liquid.

3.3.3 pH meter

It is a device used to measure the hydrogen ion activity in solutions. The acidity of a solution depends on the concentration of H^+ ions because it is responsible for the acidic properties of the compound. The sensor is immersed in the solution and then the number that appears on the screen is read.

3.3.4 Incineration

It's a piece of laboratory equipment that can achieve temperatures of up to (1200 °C), making it ideal for drying, calcining, and sintering materials. Thermostats made for this purpose regulate heating elements placed within.

3-4 Preparation of ferrite cobalt nickel($CO_{1-X}Ni_XFe_2O_4$)

Nano-nickel cobalt ferrite $CO_{1-X}Ni_XFe_2O_4$ was prepared, with values of X (0.0,0.2,0.4) respectively, according to the following steps:

1- Calculating the molecular weights of the materials:

- hydrated cobalt nitrate $CO(NO_3)_2$ $6(H_2O)$
  $58.93+(14.01+48.00)2+6(2\times1+16)=290.95$ gm

- hydrated nickel nitrate $Ni(NO_3)_2$ $6(H_2O)$
  $58.69+(14.01+48.00)2+6(2\times1+16)=290.71$ gm

- hydrated iron nitrate $Fe(NO_3)_3$ $9(H_2O)$
  $55.84+(14.01+3\times16)3+9(2\times1+16)=403.845$ gm

- Sodium hydroxide (NaOH)
  $(22.99+16.00+1.01)=40.00$ gm

2- Calculating the weights of the materials used in preparing the ferrite

Equation (1-3) was relied on to calculate the weights of the materials that were used in preparing the ferrite, as shown in Table (3-2).

$$[M]=\frac{m}{Mwt}\text{x}\frac{V}{1000} \quad \text{.....(1-3)}$$

Where M is the molar concentration, m is the mass of the solute, Mwt is the molecular weight of the solute, and V is the volume.

Table (3-2) shows the weights of the materials used to prepare (Co-Ni) ferrite

X	iron nitrate (g)	cobalt nitrate (g)	nickel nitrate (g)	Sodium hydroxide (g)
0	40.04	14.551	0	15
0.2	40.04	11.640	2.908	15
0.4	40.04	8.730	5.815	15

3.5 Co-precipitation method to prepare the ferrite-nickel-cobalt $Co_{1-x}Ni_xFe_2O_4$:

The following is a summary of the stages taken in the co-precipitation process used to generate the ferrite-nickel-cobalt complex $Co_{1-x}Ni_xFe_2O_4$ where X=(0.0,0.2,0.4):

1. Iron nitrate was dissolved in 50 ml of distilled water, cobalt nitrate is dissolved in 20 ml of distilled water, and nickel nitrate was dissolved in 20 ml of distilled water, each separately. Heat-resistant laboratory glass beakers using a magnetic stirrer for 20 minutes to obtain 100% solubility of the solutions as shown in the figure (3.1):

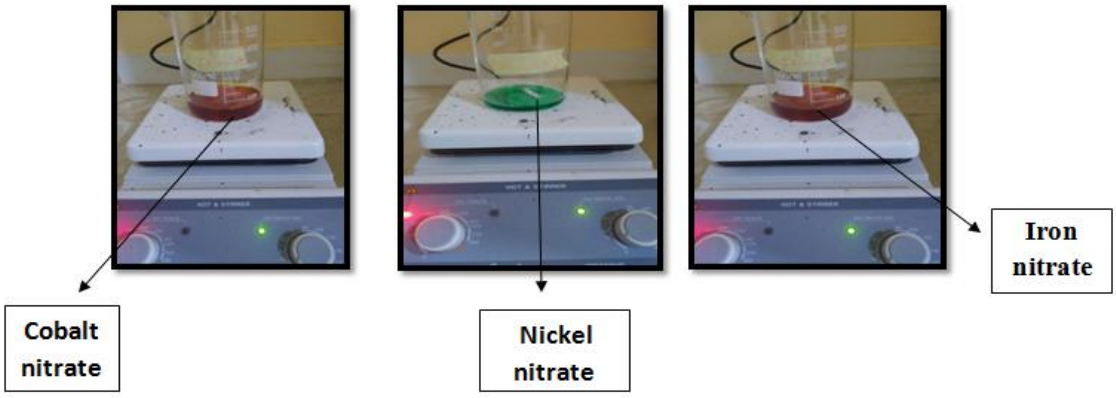

Figure (3.1): shows the stages of dissolving solutions.

2. The solutions were mixed with continuous stirring without heat for 30 minutes until we got a homogeneous mixture as in the figure (3.2):

Figure (3.2): the stage of mixing solutions and obtaining a homogeneous solution.

3. 15 g of sodium hydroxide is dissolved in 50 ml of distilled water, and then we begin to distill slowly using a burette on the homogeneous mixture and continue to stir until we get a mixture at pH = 12; while continuing to add hydroxide, , which then We need to increase the stirring time to ensure homogeneity of the final mixture.

4. After the mixture reaches PH value = 12, we heat the mixture at a temperature of 80 °C for half an hour until we get a precipitate.

5. Then the precipitate is cooled, and then the phase of washing the precipitate with deionized water begins several times to ensure the disposal of salts as shown in figure (3.3). Then the calcination process takes place at 300 ° C for 3hour to obtain the ferrite powder.

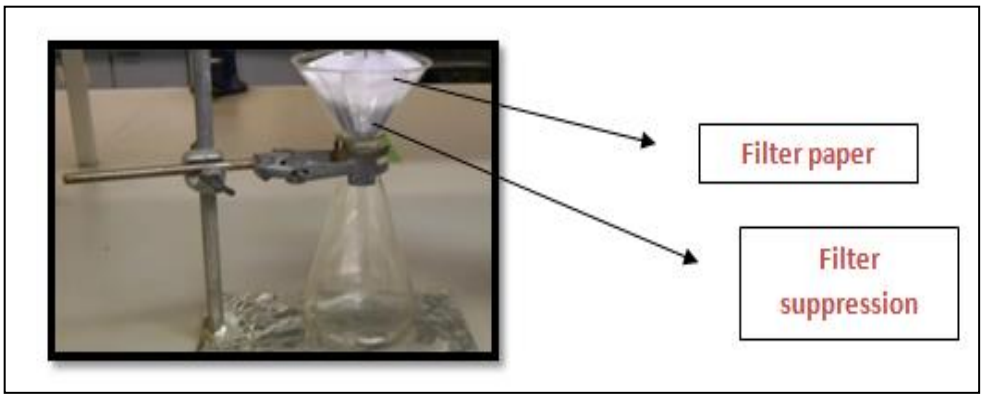

Figure (3. 3): Washing and filtering powder.

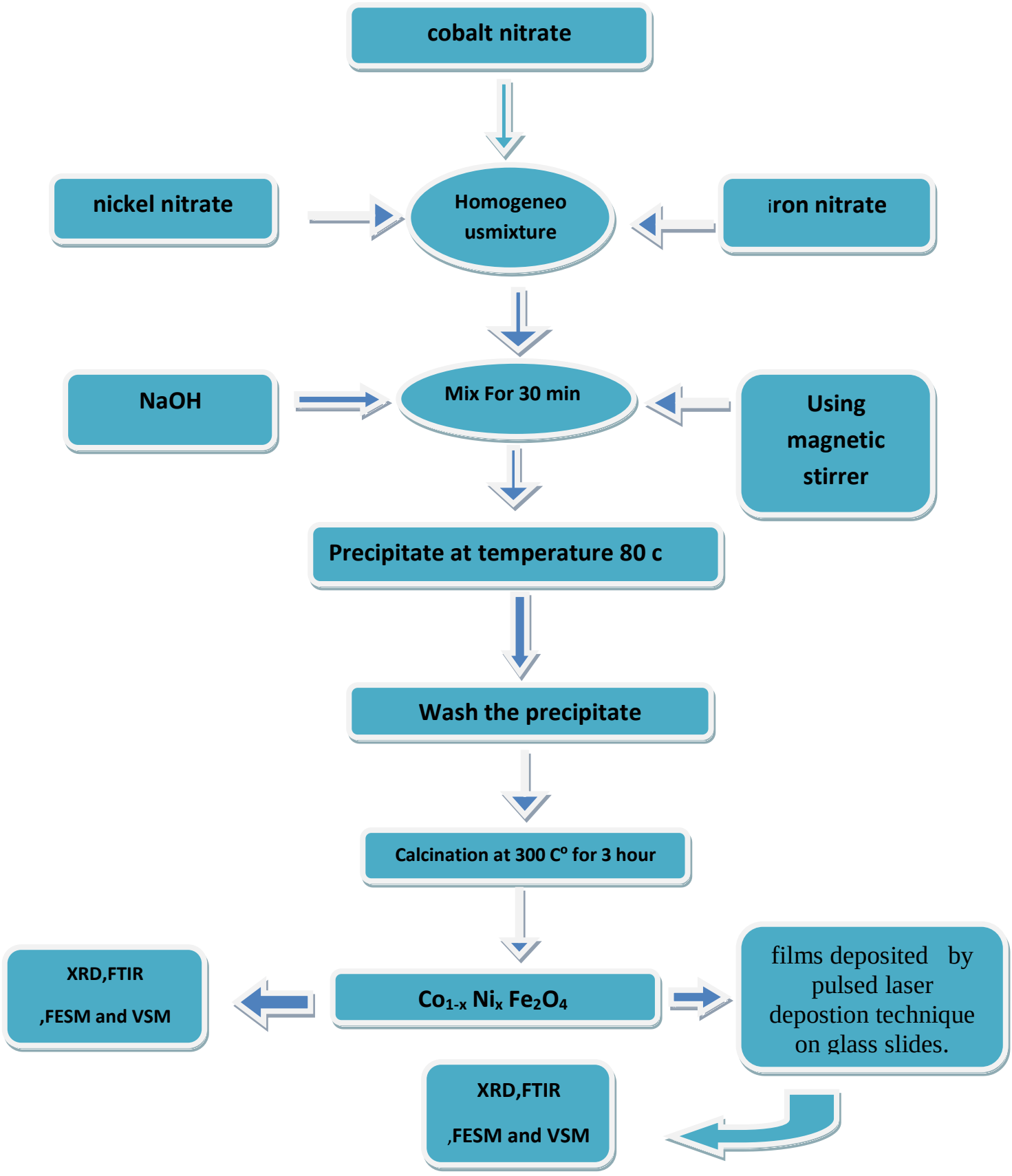

Figure (3.4): Flowchart for preparation of compound(Co_{1-x} Ni_x Fe_2O_4).

3.6 Enhance the characteristic of (Co-Ni) ferrite by Pulse laser deposition(PLD)

In this technique, Co-Ni ferrite samples must be converted to pellets, then used in laser depositions.

3.6.1 Powder compaction

The primary goal of the compaction process is to shape metal powder into compacts of the required shape that are strong enough to withstand being ejected from the tool and handled further until the end of sintering without breaking or being damaged. The final strength is imparted during the subsequent sintering process. The amount of pressure used directly relates to the density of the compacted powder. After compacting, the powder shrinks by 25 to 45 percent.

3.6.2 Pellet formation

Commonly made of hard steel, die is part of making pellet. Depending on the material's quantity, most dies produce round pellets with various diameters. The final step involved cold pressing powdered powder into pellets with a diameter of (2) cm under uniaxial pressure of 10 K psi using a steel die and a hydraulic press. Figure 3.5 depicts how a powder becomes a compact sample.

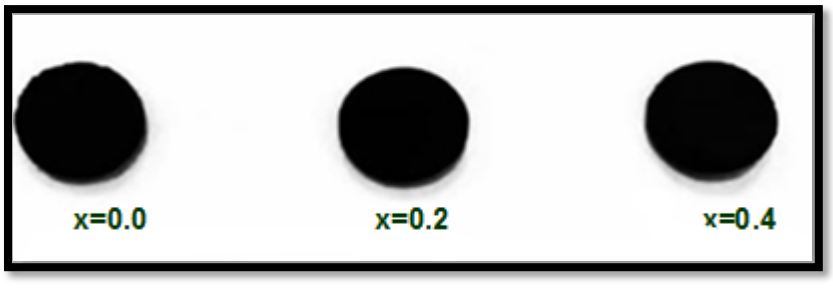

Figure (3.5): The Transformation of powder into a compact sample.

3.6.3 Pulsed Laser Deposition Technique PLD

Figure 3.6 illustrates the experimental configuration for laser ablation of a solid metal target by pulsed laser deposition. The experiment with pulsed laser deposition was typically performed in a vacuum chamber with a pressure of 3×10^{-2} Torr Nd: YAG laser's concentrated beam has a wavelength of (1064 nm) and can deliver(600 mJ). This is a repeated (pulse width 9 ns) 45-degree angle of attack using a (3 Hz)laser pulse. Both the distance from the laser to the target(10 cm) and the distance from the substrate to the target were fixed at (3cm).

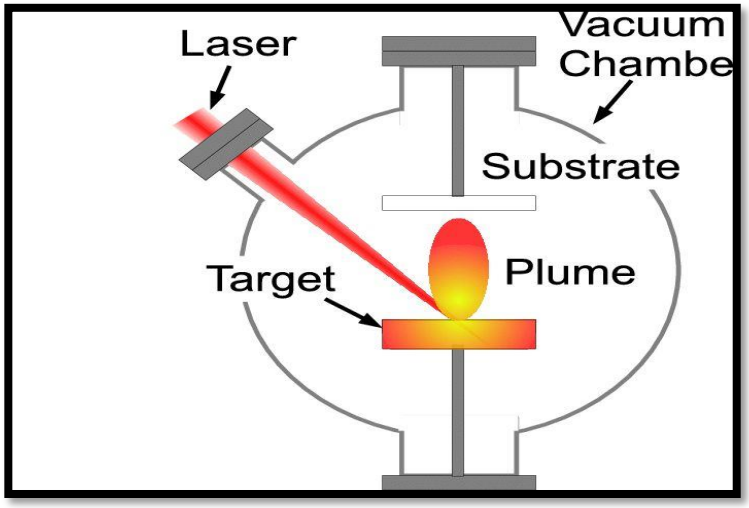

Figure(3.6): experimental setup for laser deposition.

3.7 Antibacterial test

This test was conducted in the laboratories of the Department of Biotechnology at the College of the Science / University of Diyala, where the inhibitory activity was revealed through the use of an agar well diffusion assay. The presence of a halo surrounding the holes into which the Nanomaterial was inserted is a visual representation of this inhibition. Two bacterial isolates were used in this test, including *E. coli*. and *Staphylococcus.*

3.7.1 Preparation of Mueller Hinton Agar (MHA)

Dissolve 38 mg of Mueller Hinton Agar in one liter of distilled water. Heat in stirrer ($100C^{O}$) temperature and boil for one minute to completely dissolve mueller hinton agar. Put in an autoclave at 121°C for 15 minutes. Cool to room temperature. Pour cooled Mueller Hinton Agar into sterile petri dishes on a level, horizontal surface to give uniform depth.Allow to cool to room temperature.

3.7.2 Disc diffusion method

About 20 ml of Mueller-Hinton agar was poured on sterile glass Petri dishes (90 mm) and allowed to solidify. A sterile cotton swab streaked the Agar surface of each plate with the reference bacterial strain. Paper discs of 8 mm size were impregnated in 100 µL of each sample and were placed on solidified agar plates at an equal distance with control. The plates were allowed to standby for 30 min. The plates were incubated at 37°C for 24 hours.

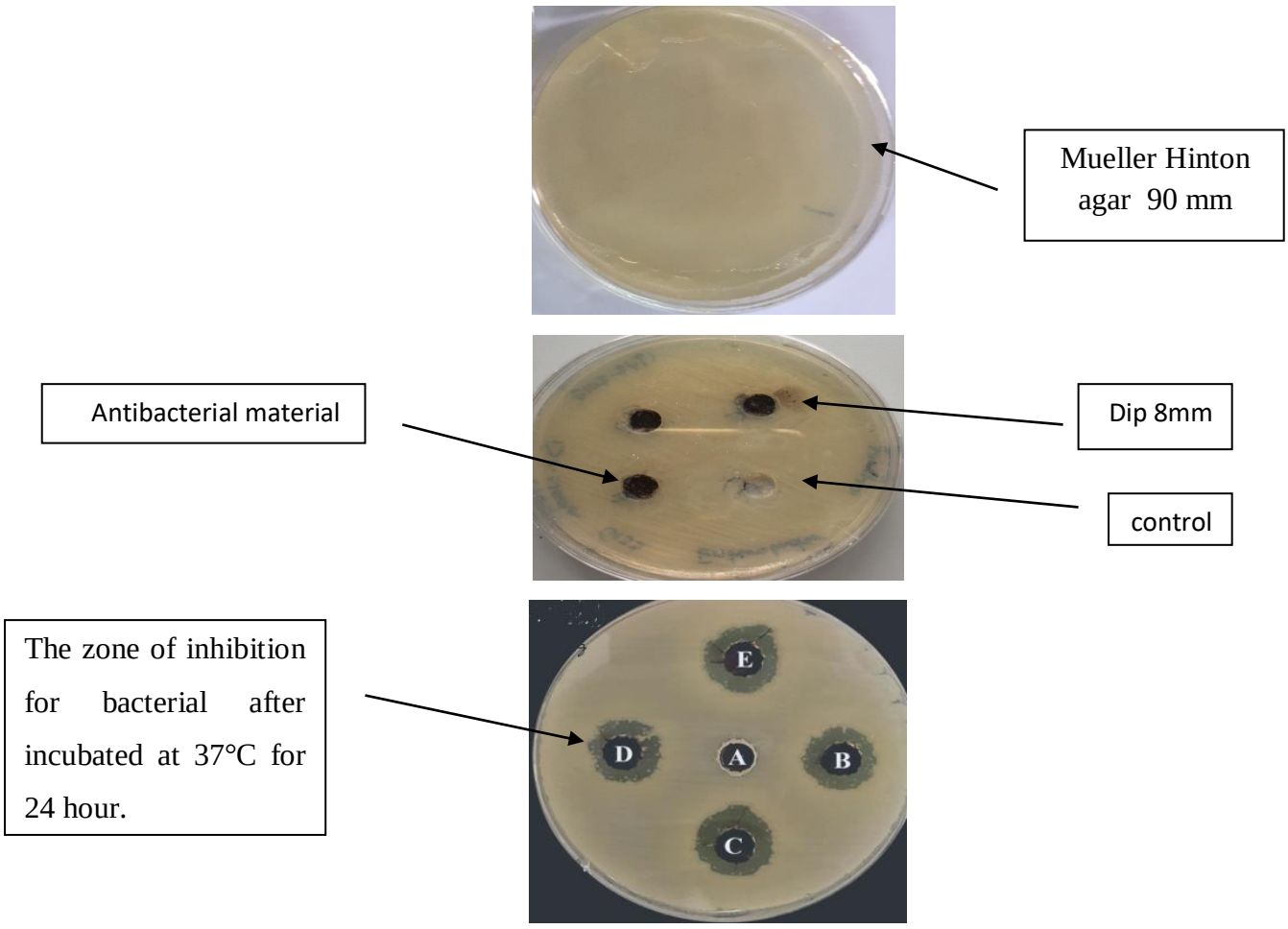

Figure 3-7: experimental setup for Disc diffusion method.

3.7.3 Bacterial examination:

The bacterial activity for the cobalt-nikel ferrite nanoparticles is tested on Gram negative Bacteria *Escherichia coli* (*E. coli*) , Gram positive Bacteria *staphylococcus* from Diyala University lab by well diffusion method with four different concentrations of the sample (100%, 75%, 50%, and 25%) which is dispersed in the distilled water solvent for the easy diffusion into the Agar. Each Well is loaded with a prepared sample solution where the plates are incubated at 37 ºC for 24 hr. , After this period zone of inhibition is observed as shown in figue(3-8). After the cuddling period ends, read the results. The positive result is the appearance of an aura of inhibition (a transparent region around the pits) . The negative result is the appearance of growth and the absence of an aura of inhibition.

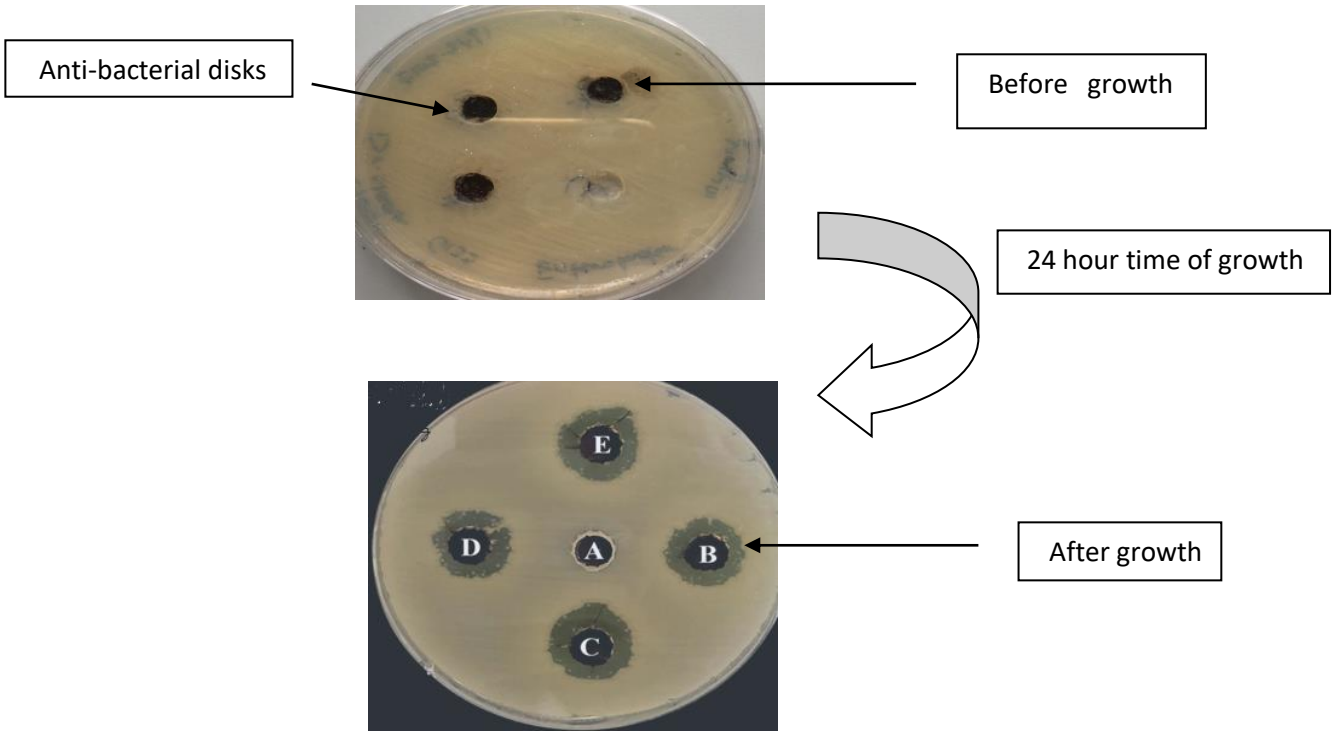

Figure 3-8: inhibition zone of bacteria.

3.8 Device test:

3.8.1 X-ray Diffraction:

Investigate the crystal structure of prepared samples at Technology university. The type of Instrument Rigaku (Ultima IV) X-ray Diffractometer.

3.8.2 Field Emission Scanning Electron Microscope.

The FESEM-MIRA3 type, developed by the Iranian firm TE-SCAN, is a field emission scanning electron microscope.

3.8.3 Fourier transform infrared spectroscopy (FTIR)

The IR spectra in the range 400-4000 cm^{-1} were recorded at room temperature using a SHIMDZU infrared spectrometer (FTIR) in Diyala university.

3.8.4 Vibrating Sample Magnetometer (VSM)

Typical Room Temperature, a vibrating sample magnetometer (VSM) can be used to precisely quantify magnetic characteristics (LBKFB model, Meghnatis Daghigh Kavir Company, Iran).

Chapter Four

Results and Discussion

4.1. Introduction

This chapter includes the results and discussions of the structural, morphological, antibacterial and magnetization properties for $Co_{1-x}Ni_xFe_2O_4$ powders prepared by co-precipitation method at different ratios x=(0.0 ,0.2 ,0.4), and for their thin films deposited by pulsed lased deposition technique on glass slides.

4.2. Structural Properties

4.2.1 XRD for Co-precipitation method

Figure 4.1 shows the XRD patterns of $Co_{1-x}Ni_xFe_2O_4$ powders prepared at different ratios by co-precipitation method and pressed at pellet. Polycrystalline cubic spinel structure of ferrite samples, with diffraction peaks located at 2θ= 18.2650°, 30.0835°, 35.4434°, 36.5690°, 43.0812°, 53.4526°, 56.9633°, 62.5912°, 71.0062°, 74.0613°, 75.0529°, and 78.9280 identical with the standard diffracted lines from (111), (220), (311), (222), (400), (422), (511), (440), (620), (533), (622), and (444) planes, respectively, corresponding to Spinal phase. These peaks identical with standard JCPDS card no. 22-1086. Small additional peaks appeared in patterns corresponding to the Fe_2O_3 Hemetite structure [97].

It seem that increasing the substitution of Ni instead of Co into the ferrite structures cause to slightly shifts in the peaks location toward higher angle, indicate on variation in lattice parameter due to the variation in ion radius. It can be seen that the crystallinety enhanced, and small variation in the lines broadening. This result agree with previous study [97], [98].

It is worth mentioning here that spinel ferrites MFe_2O_4 (where M is Zn^{2+}, Ni^{+2}, Co^{+2}) is very similar in crystal structure with little difference in lattice dimensions. This makes these compounds have nearly similar X-ray diffraction patterns with a very small shift in the location of the diffraction peaks [97], [99].

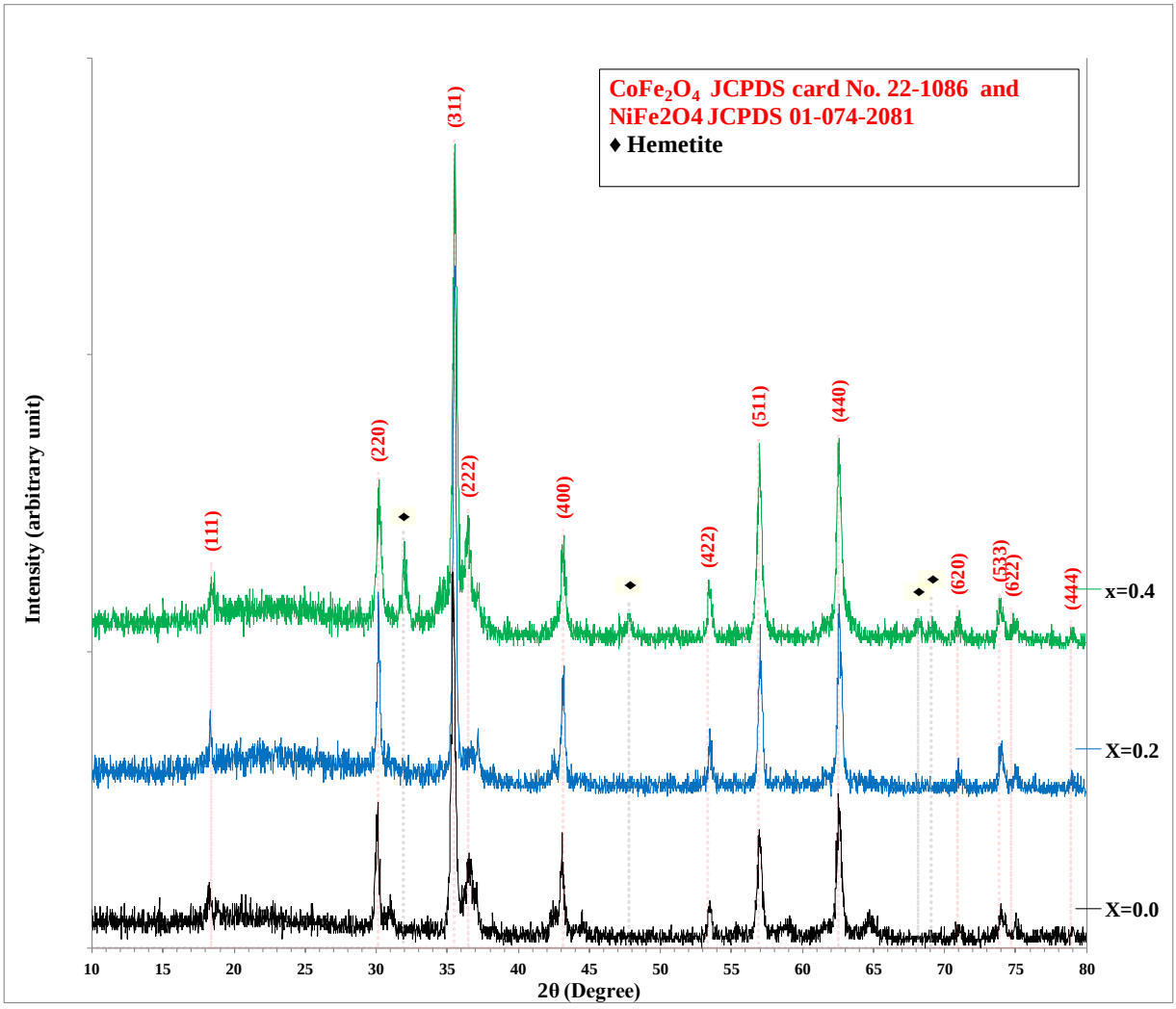

Figure 4.1: XRD patterns for $Co_{1-x}Ni_xFe_2O_4$ powders prepared at different ratios.

The inter-planer distances of the crystal layers (d_{hkl}) were calculated using the Bragg equation (2.2), while the crystal size was estimated using Scherrer equation (2.4) depending on the broadening of the diffraction lines at the half maxima (FWHM), as shown in Table 4.1. The crystal size increases at the middle ratio (X=0.2 Ni), while it decreases at the higher Ni substitution. The average crystallite sizes for $CoFe_2O_4$, $Co_{0.8}Ni_{0.2}Fe_2O_4$, and $Co_{0.6}Ni_{0.4}Fe_2O_4$ samples were 22.6, 26.6, and 25.2 nm, respectively, which are in agreement with the peak broadening.

Table 4.1: XRD parameters for $Co_{1-x}Ni_xFe_2O_4$ powders prepared at different ratios.

Sample	2θ (Deg.)	FWHM (Deg.)	d_{hkl} (Å)	D (nm)	hkl
X=0.0	18.2650	0.3752	4.8533	21.5	(111)
	30.0835	0.3484	2.9681	23.6	(220)
	35.4434	0.4288	2.5306	19.5	(311)
	36.5690	0.4556	2.4553	18.4	(222)
	43.0812	0.3484	2.0980	24.5	(400)
	53.4526	0.3752	1.7128	23.7	(422)
	56.9633	0.3484	1.6153	26.0	(511)
	62.5912	0.4020	1.4829	23.1	(440)
	71.0062	0.5092	1.3264	19.2	(620)
	74.0613	0.5360	1.2791	18.6	(533)
	75.0529	0.3216	1.2646	31.2	(622)
X=0.2	18.3346	0.2412	4.8350	33.4	(111)
	30.1531	0.2680	2.9614	30.7	(220)
	35.5130	0.2948	2.5258	28.3	(311)
	36.5850	0.4556	2.4542	18.4	(222)
	43.1508	0.3216	2.0948	26.6	(400)
	53.4954	0.3216	1.7115	27.7	(422)
	57.0597	0.3484	1.6128	26.0	(511)
	62.5804	0.4020	1.4831	23.1	(440)
	70.9686	0.4288	1.3270	22.8	(620)
	74.0237	0.3752	1.2796	26.5	(533)
	74.9349	0.4288	1.2663	23.3	(622)
	78.9280	0.3216	1.2119	32.0	(444)
X=0.4	18.4346	0.3487	4.8090	23.1	(111)
	30.1995	0.3483	2.9570	23.6	(220)
	35.5326	0.3484	2.5245	24.0	(311)
	36.4170	0.3484	2.4652	24.0	(222)
	43.1168	0.3484	2.0963	24.5	(400)
	53.4346	0.2948	1.7133	30.2	(422)
	56.9721	0.4020	1.6151	22.5	(511)
	62.5464	0.4020	1.4839	23.1	(440)
	70.9346	0.3752	1.3276	26.0	(620)
	73.8825	0.4020	1.2817	24.7	(533)
	74.8741	0.3752	1.2672	26.7	(622)
	79.0280	0.3484	1.2107	29.6	(444)

Depending on the equation (2.2) for the cubic crystalline structure [108] The lattice constant (a) was calculated from the slope of the straight line for the relationship between the values of d_{hkl} against $1/\sqrt{h^2+k^2+l^2}$, for $Co_{1-x}Ni_xFe_2O_4$ powders prepared at different ratios as shown in Figure 4.2.

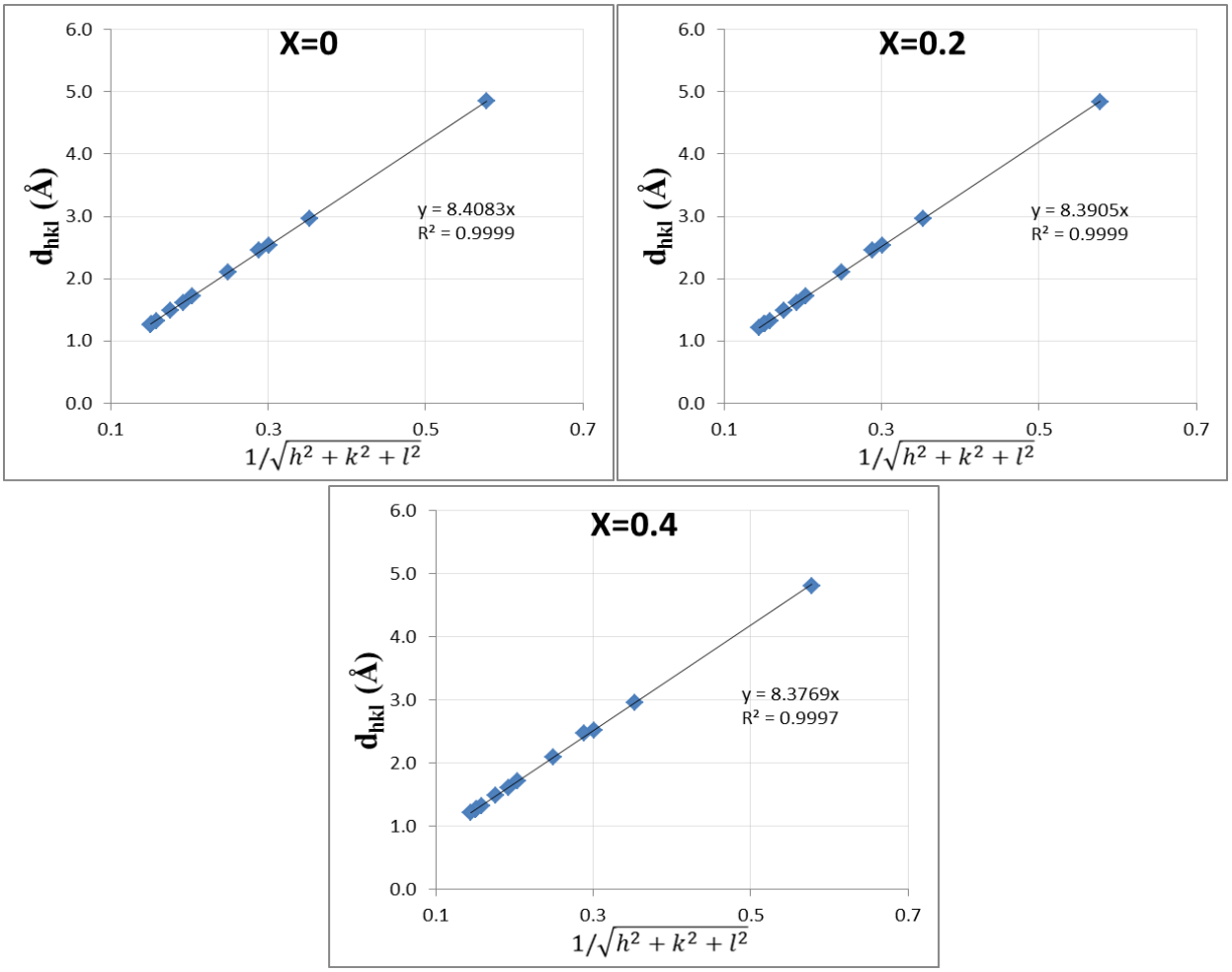

Figure 4.2: Calculation of lattice constant for spinal structure of $Co_{1-x}Ni_xFe_2O_4$ powders prepared at different ratios.

As shown in Table 4.2, the lattice parameter of the prepared cobalt ferrites was reduced linearly with the increase of Ni content from 8.408 Å to 8.377 Å. The reported lattice parameters for spinal $CoFe_2O_4$ is 8.376 Å and for spinal $NiFe_2O_4$ is

8.337 Å, while for $Co_{1-x}Ni_xFe_2O_4$ between these values [97]. The determined lattice constant values have the same behavior as it decreases with the increase of the compensated nickel percentage, but it has slightly larger values than the previously calculated values. It may be due to crystal defects as a result of presence a secondary phase that causes strain in lattice [97].

The lattice density (ρ_x) of $Co_{1-x}Ni_xFe_2O_4$ at different Ni ratio was calculated by Smith and Wijn formula equation (2.3) [100]

where N_A is the Avogadro's number, n denotes number of molecules present in the unit cell (n = 8 for spinal structure [100]) and M_w represents the molecular weight (equal the summation of ratio of each element product their atomic weight).

The variation of distance between magnetic ions in the tetrahedral A-site (L_A) and the distance between magnetic ions in the octahedral B-site (L_B) were calculated using the relations (2.5) and (2.6).

The calculated values of lattice constant (a), lattice volume(V), lattice density (ρ_x), L_A, and L_B are listed in Table 4.2. The revealed sensitivity of the ion jump lengths (L_A and L_B) on the amount of substitution of Ni instead of Co in the ferrite structure was attributed to the ionic radii mismatch variation [101]. Both L_A and L_B were reduced with increasing the Ni substitution.

Table 4.2: lattice constant (a), lattice volume (V), lattice density (ρ_x), and ion jump lengths (L_A, L_B) for $Co_{1-x}Ni_xFe_2O_4$ powders prepared at different ratios.

X	a (Å)	V(Å^3)	ρ_x(gm/cm^3)	L_A	L_B
0	8.4083	594.463	5.243	3.641	7.282
0.2	8.3905	590.695	5.276	3.633	7.266
0.4	8.3769	587.828	5.300	3.627	7.255

4.2.2 XRD for PLD method

Figure 4.3 displays the XRD patterns for $Co_{1-x}Ni_xFe_2O_4$ thin films deposited on glass slides by pulsed laser from pellet of different Ni substitution ratios. Also, Polycrystalline cubic spinel structure for the all patterns with nearly same peaks of spinal phase appeared in the powder samples with crystallinity. Additional miner phases of Hemetite (Fe_2O_3) and Magnetite (Fe_3O_4) appeared in thin film samples [97].

All the peaks have broad feature (broader than of powder samples) indicate on nano-crystalline structure. The higher crystallinity appeared at 0.2 Ni substitution ratio. Also, increasing the substitution levels of Ni instead of Co into the spinal ferrite structures cause to slightly shifts in the peaks locations toward higher diffraction angles [99].

The inter-planer distances were calculated using the Bragg equation, while the crystal size was estimated using Scherrer equation according to the diffraction lines broadening. As shown in Table 4.3, the average of crystal size of the films prepared by pulsed laser was much smaller than that of the powder samples, where the average crystallite sizes for $CoFe_2O_4$, $Co_{0.8}Ni_{0.2}Fe_2O_4$, and $Co_{0.6}Ni_{0.4}Fe_2O_4$ samples measured using the Scherrer equation were 13.7, 13.4, and 13.9 nm.

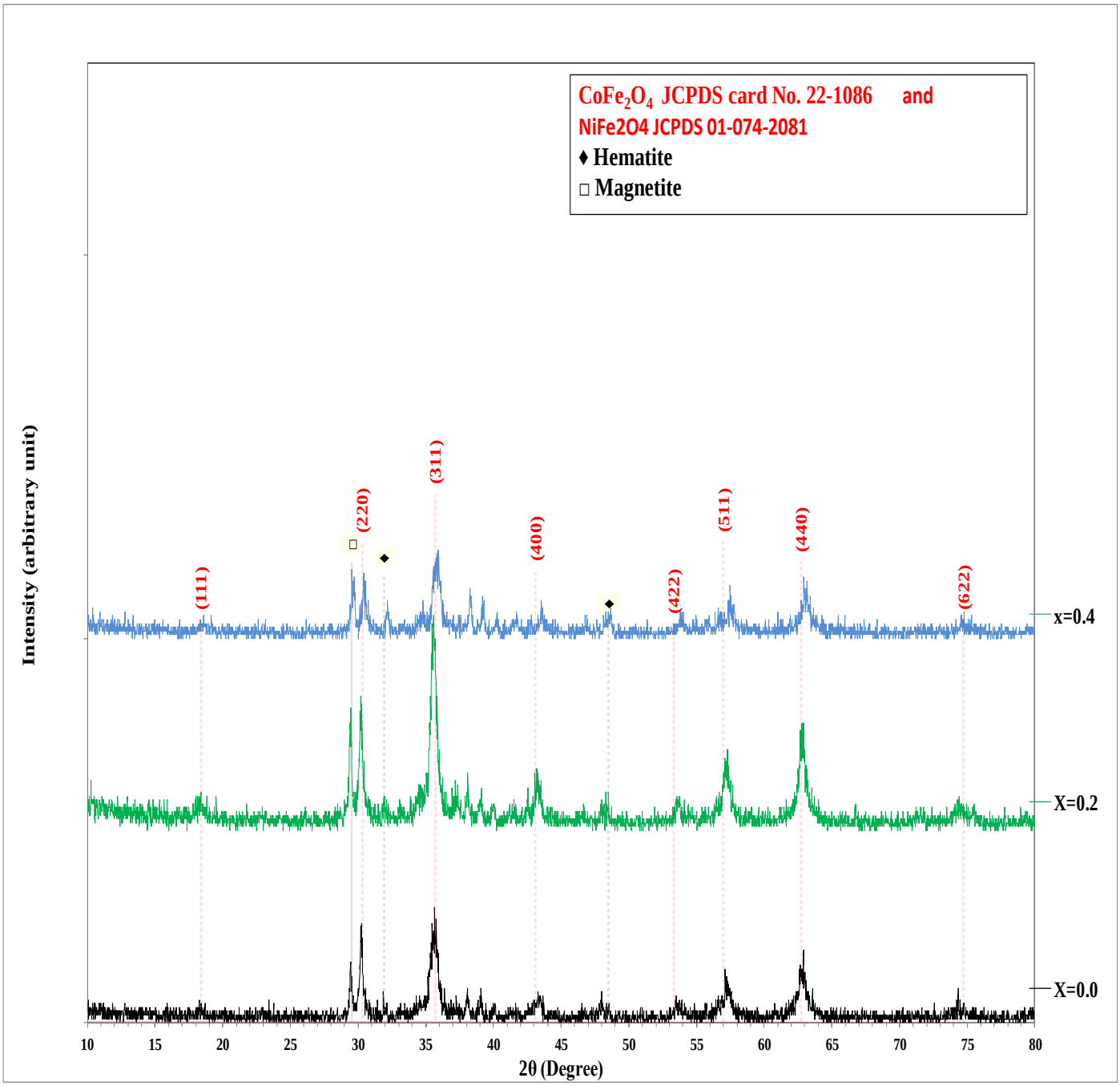

Figure 4.3: XRD patterns for $Co_{1-x}Ni_xFe_2O_4$ thin films deposited at different ratios.

Table 4.3: XRD parameters for $Co_{1-x}Ni_xFe_2O_4$ thin films prepared at different ratios.

Sample	2θ (Deg.)	FWHM (Deg.)	d_{hkl} (Å)	D (nm)	hkl
X=0	18.3571	0.6313	4.8291	12.8	(111)
	30.2810	0.3507	2.9492	23.5	(220)
	35.6818	0.7014	2.5142	11.9	(311)
	43.3271	0.7014	2.0867	12.2	(400)
	53.6377	0.7716	1.7073	11.5	(422)
	57.2148	0.7715	1.6088	11.7	(511)
	62.7559	0.7014	1.4794	13.3	(440)
	74.3291	0.7716	1.2751	12.9	(622)
X=0.2	18.4168	0.7716	4.8136	10.4	(111)
	30.2705	0.4209	2.9502	19.6	(220)
	35.5311	0.5612	2.5246	14.9	(311)
	43.2465	0.6312	2.0904	13.5	(400)
	53.6974	0.7014	1.7056	12.7	(422)
	57.1343	0.6313	1.6109	14.3	(511)
	62.8156	0.7014	1.4781	13.3	(440)
	74.4589	1.1924	1.2732	8.4	(622)
X=0.4	18.5571	0.6312	4.7775	12.8	(111)
	30.4810	0.4910	2.9303	16.8	(220)
	35.9519	0.7014	2.4960	11.9	(311)
	43.5271	0.4910	2.0775	17.4	(400)
	53.9078	0.5611	1.6994	15.9	(422)
	57.4850	0.7015	1.6019	12.9	(511)
	63.0261	0.9118	1.4737	10.2	(440)
	74.6693	0.7716	1.2701	13.0	(622)

The lattice constant (a) was calculated from the slope of the straight line for the relationship between the values of d_{hkl} against $1/\sqrt{h^2+k^2+l^2}$, for $Co_{1-x}Ni_xFe_2O_4$ thin films prepared at different Ni content as shown in Figure 4.4.

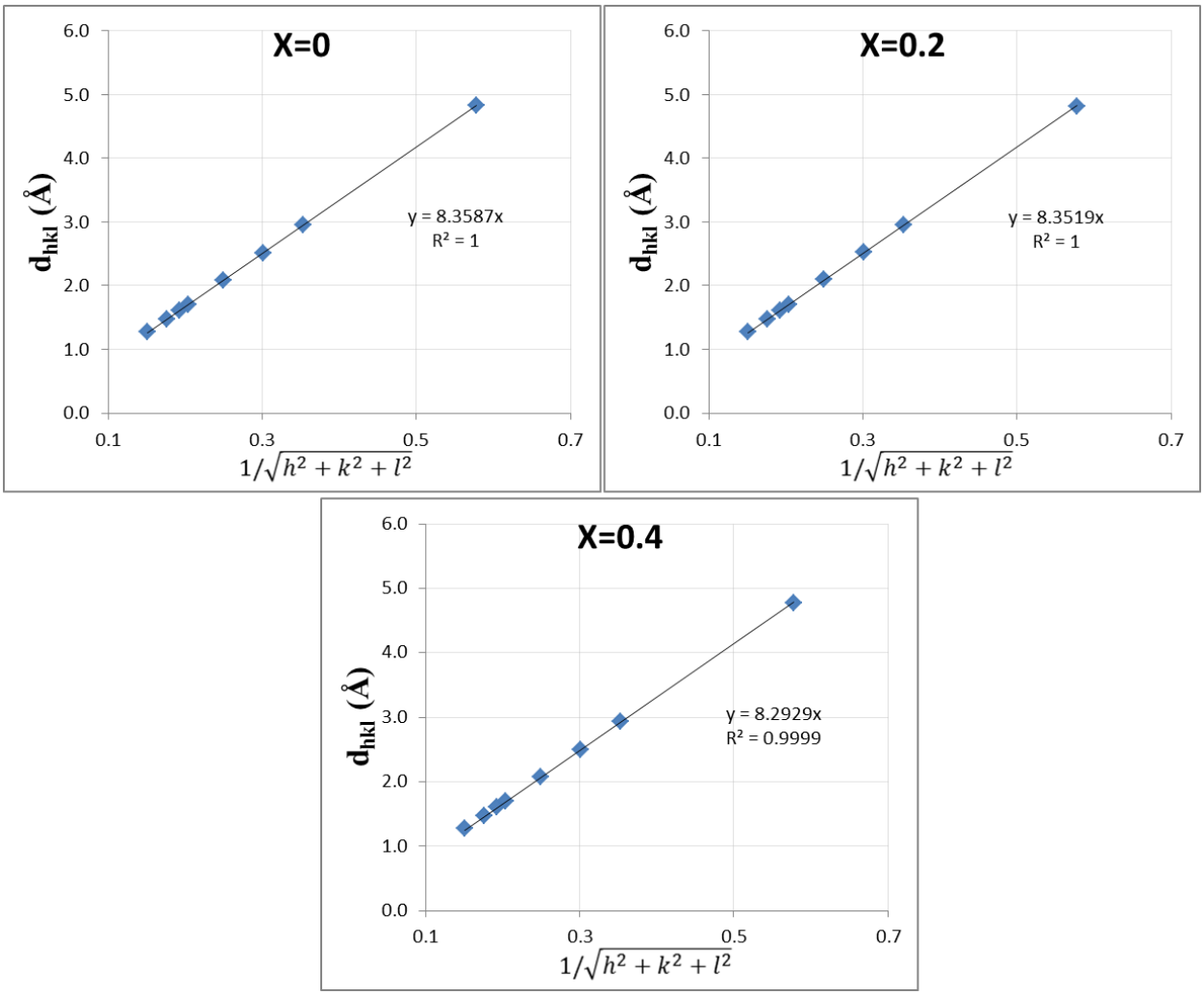

Figure 4.4: Calculation of lattice constant for spinal structure of $Co_{1-x}Ni_xFe_2O_4$ thin films deposited at different ratios.

As shown in Table 4.4, the lattice parameter of the prepared cobalt ferrites was reduced from 8.3587 Å to 8.2929 Å with increasing the Ni substitution from 0 to 0.4. The determined lattice constant values for the thin film samples have the same behavior as decreases with the increase of the substituted Ni ratio as in powder samples. The variation of ion jump lengths (L_A and L_B) were calculated using the relations 4.3 and 4.4. The calculated values of a, V, ρ_x, L_A, and L_B are listed in Table 4.4. It seems that both L_A and L_B were reduced with increasing the Ni substitution.

Table 4.4: lattice constant (a), lattice volume (V), lattice density (ρ_x), and ion jump lengths (LA, LB) for $Co_{1-x}Ni_xFe_2O_4$ thin films prepared at different ratios.

X	a (Å)	V(Å^3)	ρ(gm/cm^3)	L_A	L_B
0	8.3587	584.005	5.337	3.619	7.239
0.2	8.3519	582.580	5.349	3.616	7.233
0.4	8.2929	570.321	5.463	3.591	7.182

4.3. Furrier Transform Infra-red spectroscopy

4.3.1 FTIR for Co-precipitation method

Figure 4.5 displays the FTIR transmission patterns for $Co_{1-x}Ni_xFe_2O_4$ ferrite powders prepared by co-precipitation method at different Ni-Co substitution ratios at the range of 400 to 4,000 cm^{-1}. All the spinel ferrites have two significant absorption bands [102]. The highest frequency bands corresponding to the vibrations of the metal oxide (Fe^{3+}-O^{2-}) at the tetrahedral site (site A), and the lowest frequency one correspond to octahedral trivalent metal-oxide stretching (site B) in the wavenumber range 400 to 700 cm^{-1} [103]. For the $Co_{1-x}Ni_xFe_2O_4$ the substituted Ni^{+2} occupies into the octahedral site. The difference of band positions between the two vibrations due the difference in the M-O distance for the octahedral and the tetrahedral sites [104].

All the spectrum display two significant frequency bands at 576.71 cm^{-1} and 405.97 cm^{-1} corresponding to M-O bond. These bands reveal the synthesize of spinel ferrite structure, which is in agreement with the XRD data. Increasing the Ni substitution cause to small shift of these absorption bands toward higher frequencies due to decreasing the bond length of L_A and L_B, as shown by the X-ray diffraction [105].

The absorption bands around 3400 and 1600 cm^{-1} correspond to the stretching and the vibration modes of the O−H band, respectively [103]. The absorption bands at

around 3140, 1788, 1379, 882, and 833.96 cm^{-1}, as shown in Table 4.5, corresponding to C-H Stretching, C=O stretching, C-O, and C-H bending, respectively, comes from residual elements of preparation precursors [106].

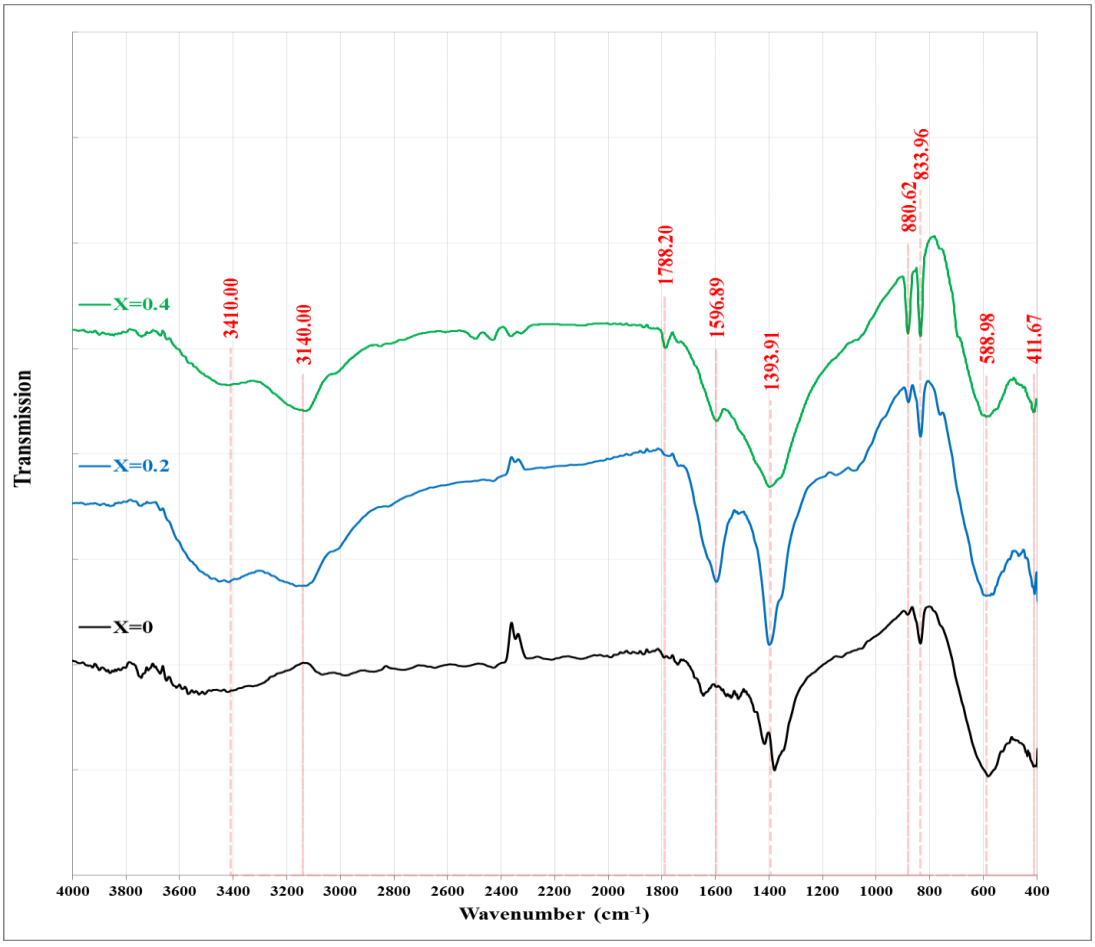

Figure 4.5: FTIR patterns for $Co_{1-x}Ni_xFe_2O_4$ powders at different ratios.

Table 4.5: FTIR bands for $Co_{1-x}Ni_xFe_2O_4$ powders at different ratios.

Band type	X=0	X=0.2	X=0.4
O-H stretching	-	3410.00	3410.00
C-H Stretching	-	3140.00	3140.00
C=O stretching	-	-	1788.20
O-H bending	1645.88	1596.89	1596.89
C-O	1379.91	1396.24	1393.91
C-H	882.96	878.29	880.62
	833.96	833.96	833.96
Fe-O (Tetra.)	576.71	583.69	585.70
Fe-O (Octa.)	405.97	408.99	411.67

4.3.2 FTIR for PLD method

Figure 4.6 shows the FTIR patterns for $Co_{1-x}Ni_xFe_2O_4$ thin films prepared by PLD technique at different Ni ratios at the range of 400 to 4000 cm^{-1}. The patterns have nearly the same bands as in powder sample. The two vibration bands of ferrite locate around 581, and 406 cm^{-1} also behave to increase in energy with increasing the Ni contents, but with higher values than that for powder samples, as shown in Table 4.6, because the values of L_A and L_B in thin films are less than in powder samples, as indicated by the analysis of XRD data.

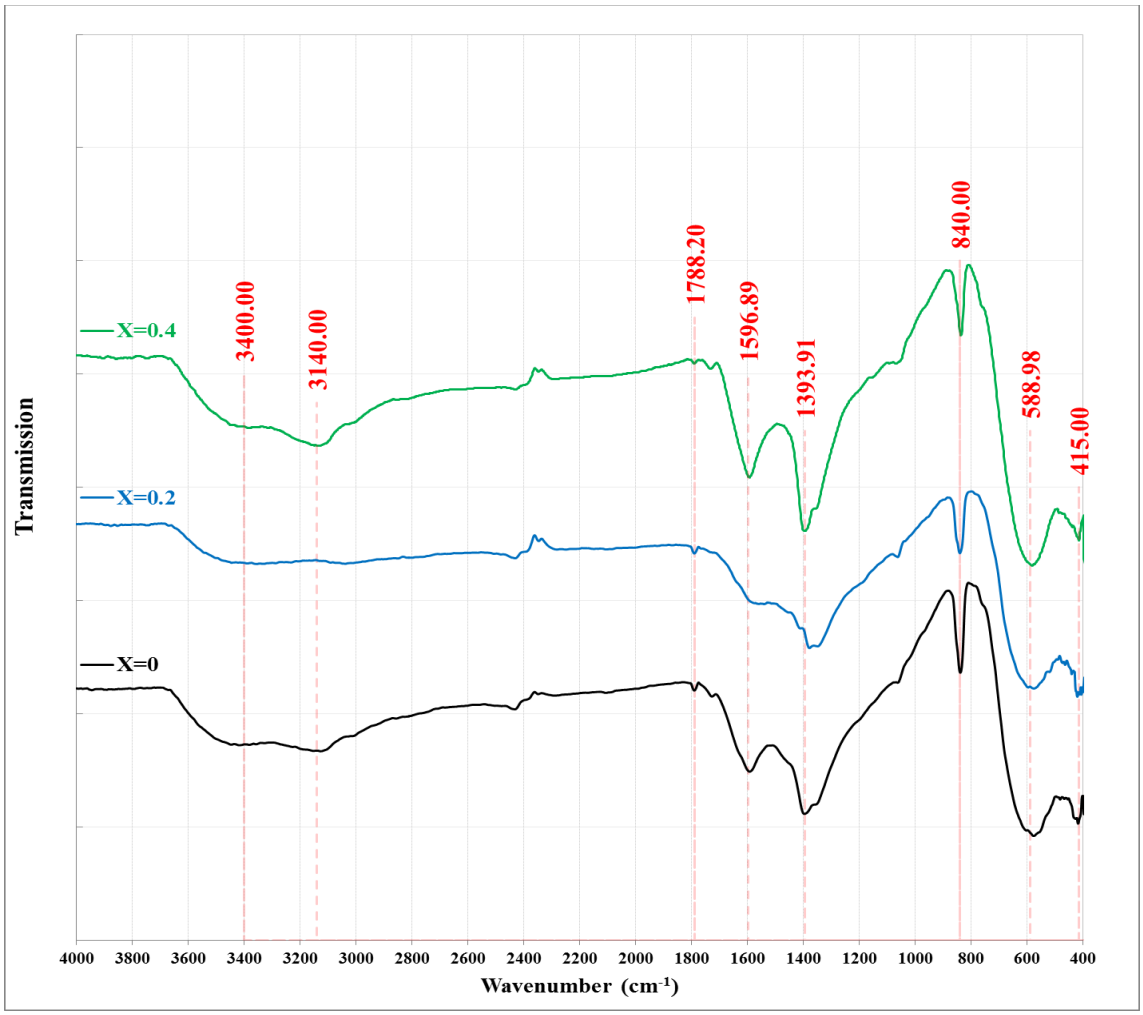

Figure 4.6: FTIR patterns for $Co_{1-x}Ni_xFe_2O_4$ thin films at different ratios.

Table 4.6: FTIR bands for $Co_{1-x}Ni_xFe_2O_4$ thin films at different ratios.

Band type	X=0	X=0.2	X=0.4
O-H stretching	3400.00	3400.00	3400.00
C-H Stretching	3140.00	-	3140.00
C=O	1789.68	1789.65	1789.62
O-H bending	1595.01	1586.02	1595.01
C-O	1397.34	1379.37	1394.34
C-H	837.27	840.27	837.27
Fe-O	581.98	584.32	588.98
Fe-O	406.33	409.33	414.98

4.4. Field Emission Scanning Electron Microscopy

4.4.1 FE-SEM for Co-precipitation method

The surface morphological of $Co_{1-x}Ni_xFe_2O_4$ powder samples at different Ni contents were examined by field emission scanning electron microscopy (FE-SEM) as shown in Figures 4.7, at two magnification powers (10 kX and 200 kX) for each sample. The powder sample appeared as irregular rock behavior with laminar crystal structure, as shown in previous study [107]. The structure mixed with solid mass of structure and attached with small spherical particles within the range of (21-23 nm) diameter. The grain size of these particles was measured from FE-SEM image by using the image-j software.

The uniform nature of the ferrite particle is showing fine grain growth in the samples along with some agglomeration. It is clear from the FE-SEM micrographs that the microstructure changes with Ni^{+2} substitution. Also, it is observed that with the substitution of Ni porosity is observed to increase, the individual grains are parted from each other and the effective area of grain contact decreases.[108]

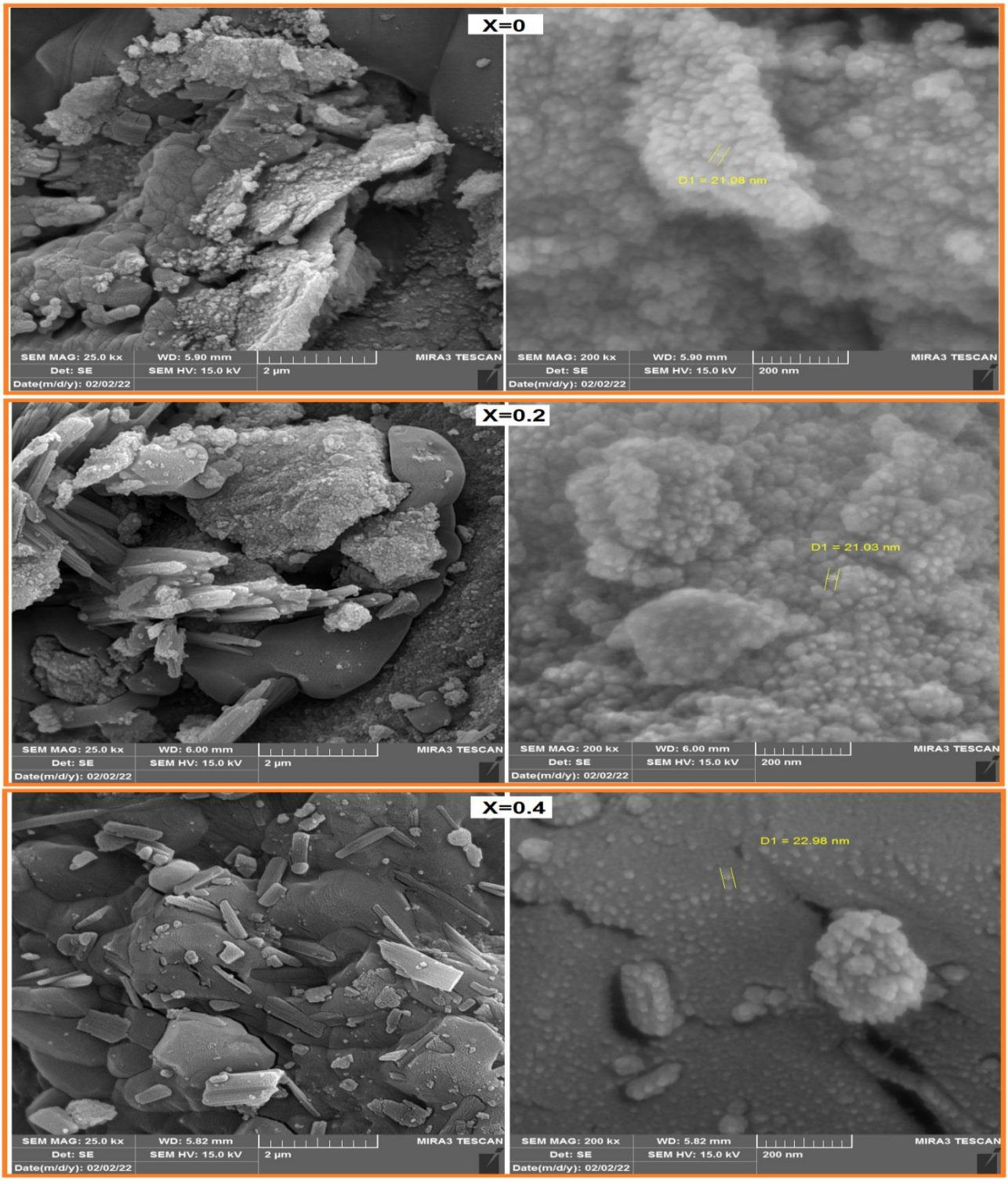

Figure 4.7: FE-SEM images at two magnification powers for $Co_{1-x}Ni_xFe_2O_4$ powders prepared at different ratios.

4.4.2 FE-SEM for PLD method

The surface morphological of $Co_{1-x}Ni_xFe_2O_4$ thin films at different Ni substitution were tested by FE-SEM as shown in Figures 4.8, at two magnification powers (10 kX and 200 kX). The $CoFe_2O_4$ thin films samples appeared as mix of nanoribbons and flakes shapes structure. These nanostructures are similar to those obtained by previous study [109]. The nanoribbons has diameter of range from 130 to 300 nm and with a few micrometers in length and some nanometer thickness. The entire surfaces of these structure covered with spherical nanoparticles of about 20 nm diameter.

The $Ni_{0.2}Co_{0.8}Fe_2O_4$ thin films samples appeared as mix nanoribbons of laminar crystalline block structure .

Increasing the Ni content to 0.4 in thin-film samples makes the sample appear a massive porous structure. The variation of nanostructure behavior of the samples with the ratio of nickel is due to the different tendency of the ions to bond at different angles that are as a seeds to growth the thin film sample.

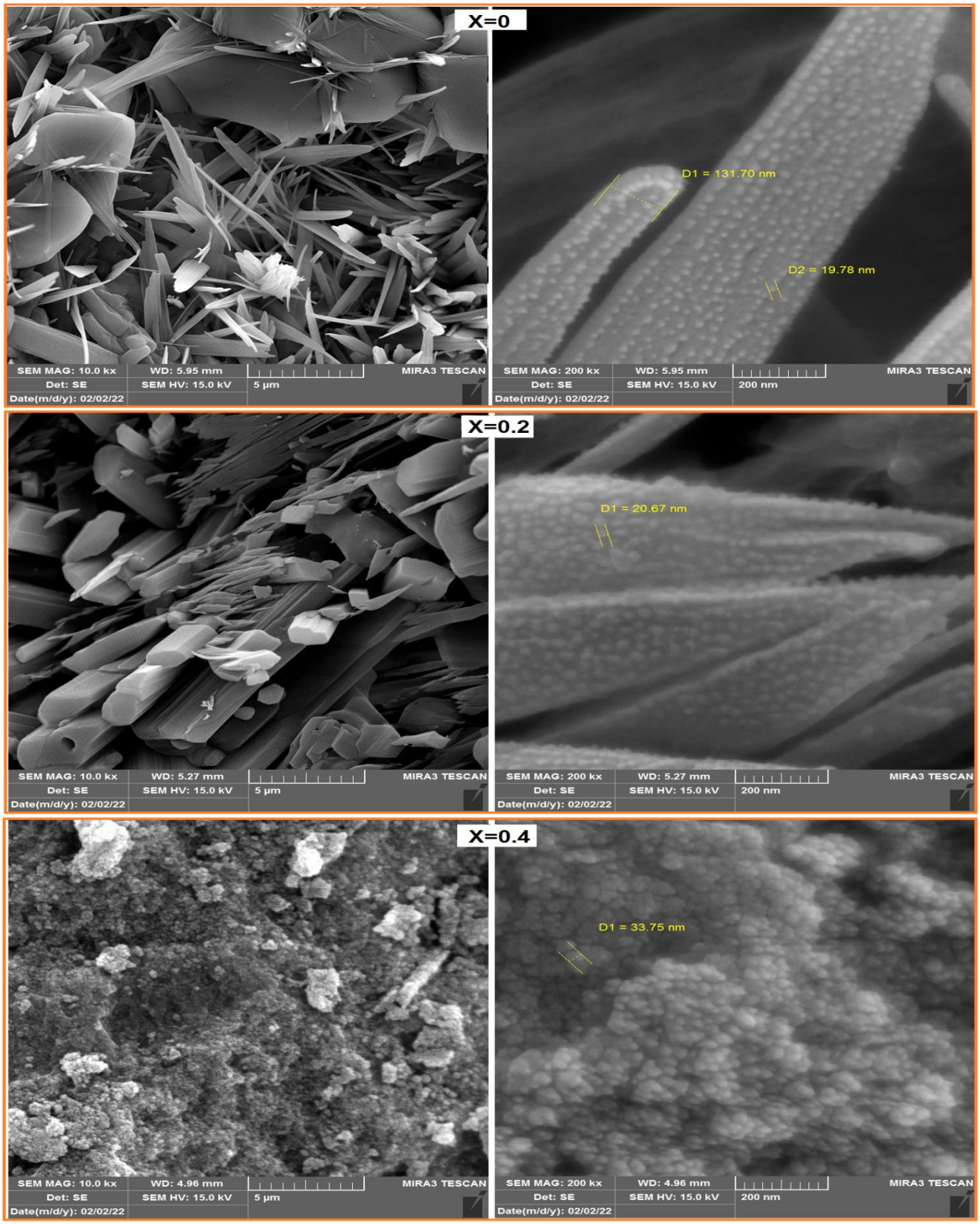

Figure 4.8: FE-SEM images at two magnification powers for $Co_{1-x}Ni_xFe_2O_4$ thin films deposited at different ratios.

4.5. Magnetic Properties

4.5.1 VSM for Co-precipitation method

The magnetic property test of $Co_{1-x}Ni_xFe_2O_4$ ferrite powders, prepared by co-precipitation method at different Ni-Co substitution ratios, tested using vibrating sample magnetometer (VSM) were shown in Figure 4.9. All samples showed a typical S-shaped hysteresis ring. The hysteresis loop area decrasing in addition to decrase the slope of first linear part (indicating decrasing the susceptibility) with increasing the Ni ratio.

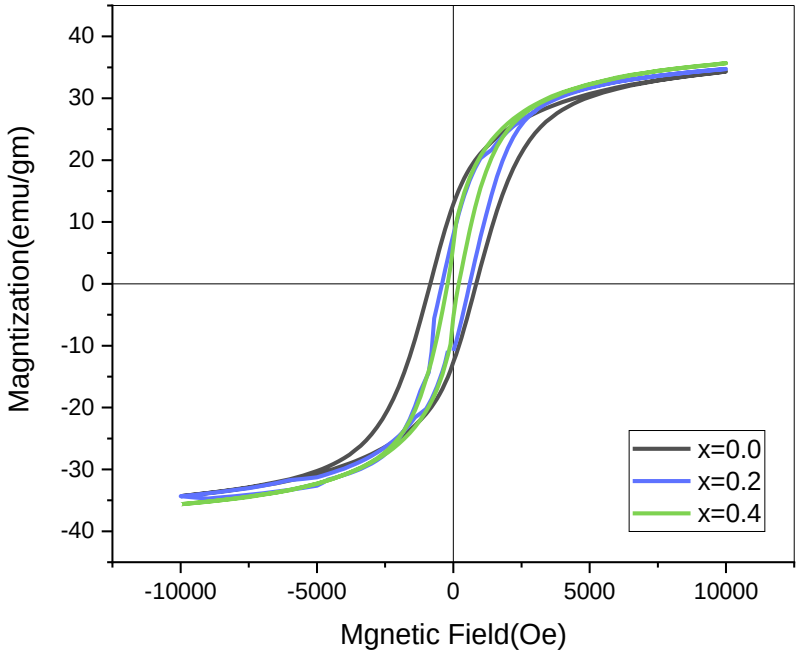

Figure 4.9: The magneto-hysteresis loop for $Co_{1-x}Ni_xFe_2O_4$ powders prepared at different ratios.

Figure 4.10 illustrate the variation of residual magnetization (M_r) and the coercive field (H_c) for $Co_{1-x}Ni_xFe_2O_4$ with Ni ratio for powder and thin films samples for respectively. It is clearly that M_r , H_c decrasing with increasing the Ni content. Table 4.7 shows the VSM parameters for the powder samples.

These plots shows that the increase in Ni^{2+} content reduces the magnetization(M_s) of Co–ferrite, which due to the substitution of Ni^{2+} ions by Co^{2+} ions on the octahedral sites. The magnetic moment n_B per 8 ions for Co^{2+} ions (3 µB) is more than that for Ni^{2+} ions (2 µB). Therefore, the decreasing Co^{2+} concentration on the octahedral sites result in a decreasing magnetic moment per formula of $Co_{1-x}Ni_xFe_2o_4$.

Figure 4.9 shows that coercivity reduced from 850 Oe to 200 Oe for higher Ni content and it is important to keep a high magnetization when the coercivity is reduced [110]. In the this case, coercivity is decreased at the cost of small decrease in magnetization, which suggests its suitability for medical applications.

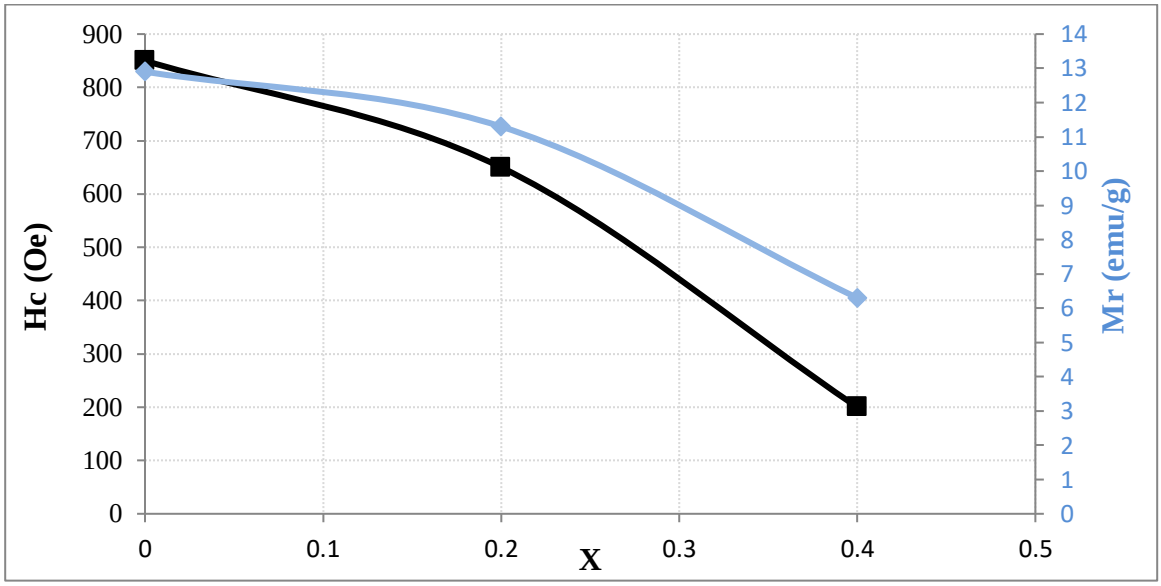

Figure 4.10: variation of residual magnetization and coercive field for $Co_{1-x}Ni_xFe_2O_4$ powder at different ratios.

Table 4.7.: Magnetization parameters for $Co_{1-x}Ni_xFe_2O_4$ powder at different ratios.

X	M_r (emu/g)	H_c (Oe)	M_s (emu/g)	Mr/Ms
0	12.9	850	35.5	0.363
0.2	11.3	650	34.8	0.324
0.4	6.3	200	34.3	0.183

4.5.2 VSM for PLD method

Figure 4.11 shows the VSM test for $Co_{1-x}Ni_xFe_2O_4$ ferrite thin film, prepared by PLD at different Ni contents on glass slides. Also, typical hysteresis loop appeared for the thin film samples but with less area when compare with the powder sample. Similarly, the hysteresis loop area decrasing with increasing the Ni ratio. The coercive field (Hc), residual magnetization (Mr), and saturation magnetization (Ms), for the powder and thin films samples, were extrapolated from the two figures and included in Table 4.8. All these parameters decreasing, with increasing the Ni content .

Figure (4.11) shows the variation of magnetization as a function of applied magnetic field at room temperature for $Co_{1-x}Ni_xFe_2O_4$ samples was studied using VSM curve. The magnetization curve for x= 0 has a small broad result of small coercivity while x= 0.2 and **x**= 0.4 clearly trace an 'S' shape, which indicating virtually no thermal effect from hysteresis loss would be expected for these materials. coercivity Hc and magnetazation Ms is drastically decreases. The reduction in size of ferrite nanoparticles will enhance the super-paramagnetic behavior. One of the important reasons for this enhancement will be the migration of Fe^{+3} ions into the tetrahedral site, which eventually restructure the magnetic interaction between the octahedral as well as tetrahedral sites. In order to explain the effect of reducing domain, squareness ratio (Mr/Ms) was calculated for each sample [111],[112].

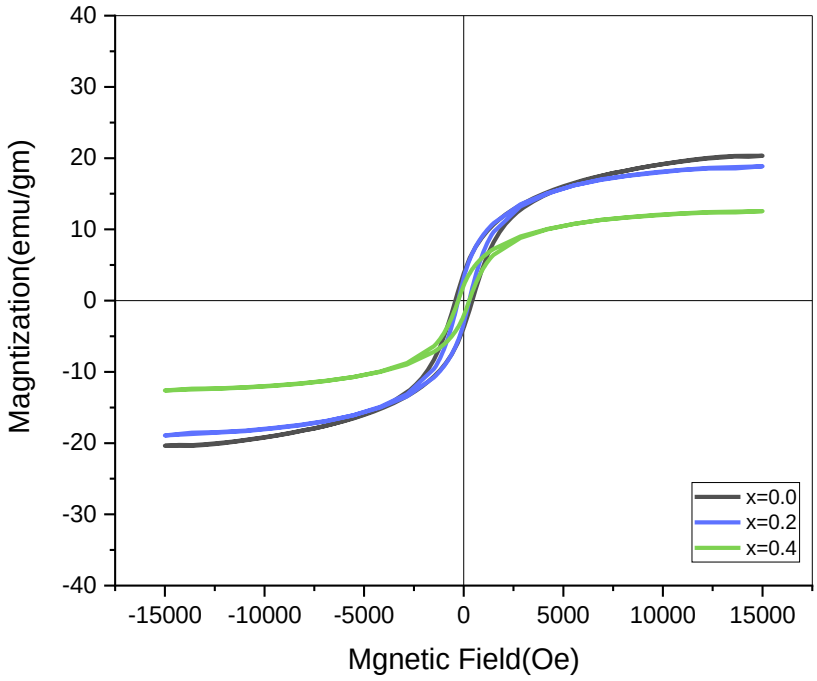

Figure 4.11: The magneto-hysteresis loop for $Co_{1-x}Ni_xFe_2O_4$ thin films deposited at different ratios.

Table 4.8.: Magnetization parameters for $Co_{1-x}Ni_xFe_2O_4$ thin films at different ratios.

X	M_r (emu/g)	H_c (Oe)	M_s (emu/g)	Mr/Ms
0	3.82	450	20	0.191
0.2	3.19	285	18.9	0.168
0.4	2.13	220	12.5	0.170

Figure 4.12 illustrates the variation of residual magnetization (M_r) and the coercive field (H_c) for $Co_{1-x}Ni_xFe_2O_4$ with the Ni ratio for thin films samples. Both M_r and H_c decreasing with increasing the Ni content. It seems that both magnetic parameters thin film samples more than powder samples as its bulk form of large substance.

The determined value of *Mr* and *Ms* (in two form powder and thin films) of large values and varying with the Ni substitution ascribed to the existence of strong exchange interactions among the ions that occupied the tetrahedral and the octahedral sites. The reducing of lattice parameter also confirmed the strong ionic interactions among various lattice sites [97].

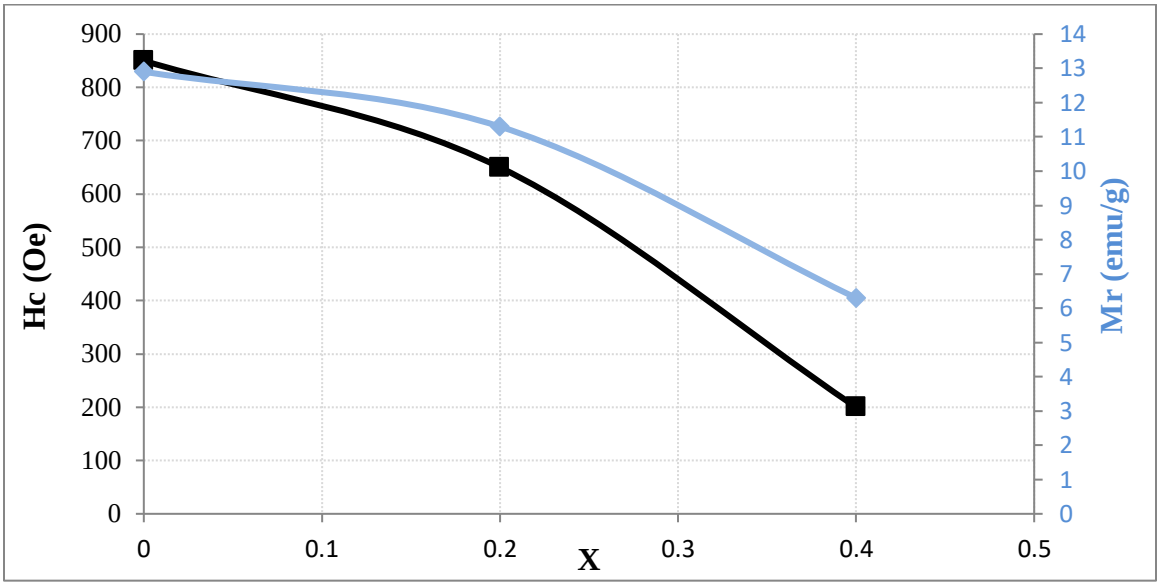

Figure 4.12: variation of residual magnetization and coercive field for $Co_{1-x}Ni_xFe_2O_4$ thin films at different ratios.

4.6. Antibacterial activity of $Co_{1-x}Ni_xFe_2O_4$

The antibacterial potential of $Co_{1-x}Ni_xFe_2O_4$ powder and thin films was investigated against Gram's negative (*E.coli*) and Gram's positive (*S.aureus*) bacterial (the most prevalent clinically resistant pathogenic bacteria) using agar well diffusion assay. About 20 mL of on Muller–Hinton (MH) agar was aseptically poured into sterile Petri dishes. The bacterial species were collected from their stock cultures using a sterile wire loop. After culturing the organisms, 6 mm-diameter wells were bored on the agar plates using of a sterile tip. Into the bored wells, different concentrations of the sample (100%, 75%, 50%, and 25%) were used. The cultured plates containing the $Co_{1-x}Ni_xFe_2O_4$ samples and the test organisms were incubated

overnight at 37 °C before measuring and recording the average the zones of inhibition diameter.

4.6.1 Antibacterial activity for Co-precipitation method

Figure 4.13 shows antibacterial activity test of $Co_{1-x}Ni_xFe_2O_4$ powders at different Ni content against *E.coli*. The highest inhibitory activity appeared for the sample prepared for the 0.4 Ni ratio sample with 30 mm inhibition zone diameter.

Figure 4.14 displays the antibacterial potential test for the $Co_{1-x}Ni_xFe_2O_4$ powders at different Ni content against *S.aureus* bacteria. The highest antibacterial activity appeared for the $CoFe_2O_4$ sample with 33 mm inhibition zone diameter for the100% concentration, and reduced to 27 mm inhibition zone for 25% concentration.

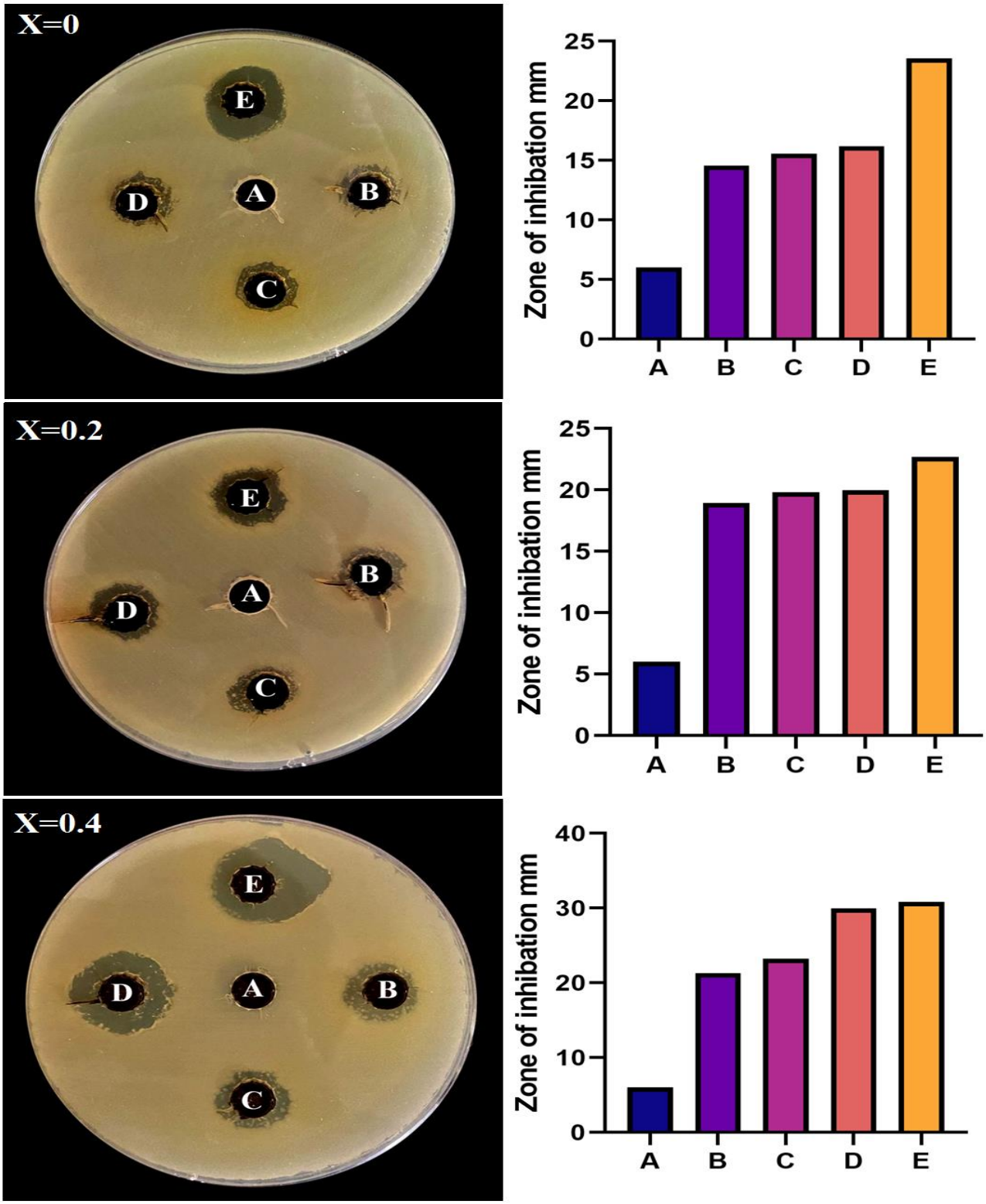

Figure 4.13: Antibacterial activity of $Co_{1-x}Ni_xFe_2O_4$ powders at different Ni content against *E.Coli* . A, control. B, 25%. C, 50%. D, 75%. E, 100%.

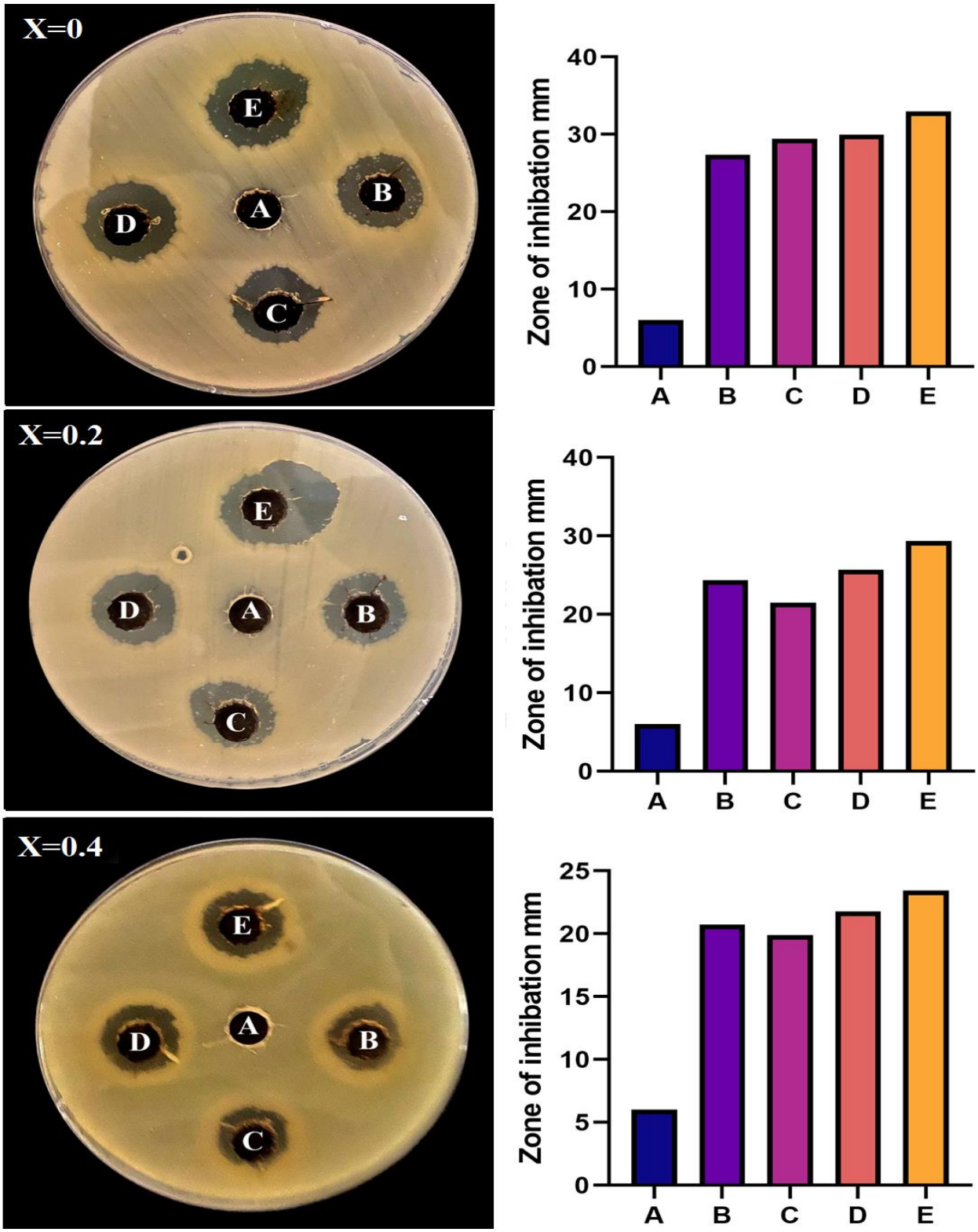

Figure 4.14: Antibacterial activity of $Co_{1-x}Ni_xFe_2O_4$ Powder at different Ni content against *S. aureus*.A, control. B, 25%. C, 50%. D, 75%. E, 100%.

4.6.2 Antibacterial activity for PLD method

Figure 4.15 shows antibacterial activity test of $Co_{1-x}Ni_xFe_2O_4$ thin films at different Ni content against *E.Coli*. Also, the highest antibacterial activity appeared for the highest Ni ratio sample with 30 mm inhibition zone diameter and few reduced to 27 mm when diluted the sample to 25%.

Figure 4.16 shows antibacterial activity test of $Co_{1-x}Ni_xFe_2O_4$ thin films at different Ni content against *S.aureus*. The highest antibacterial activity appeared for the $CoFe_2O_4$ sample with 32 mm inhibition zone inhibition zone diameter and reduced to 22 mm when diluted the sample to 25%.

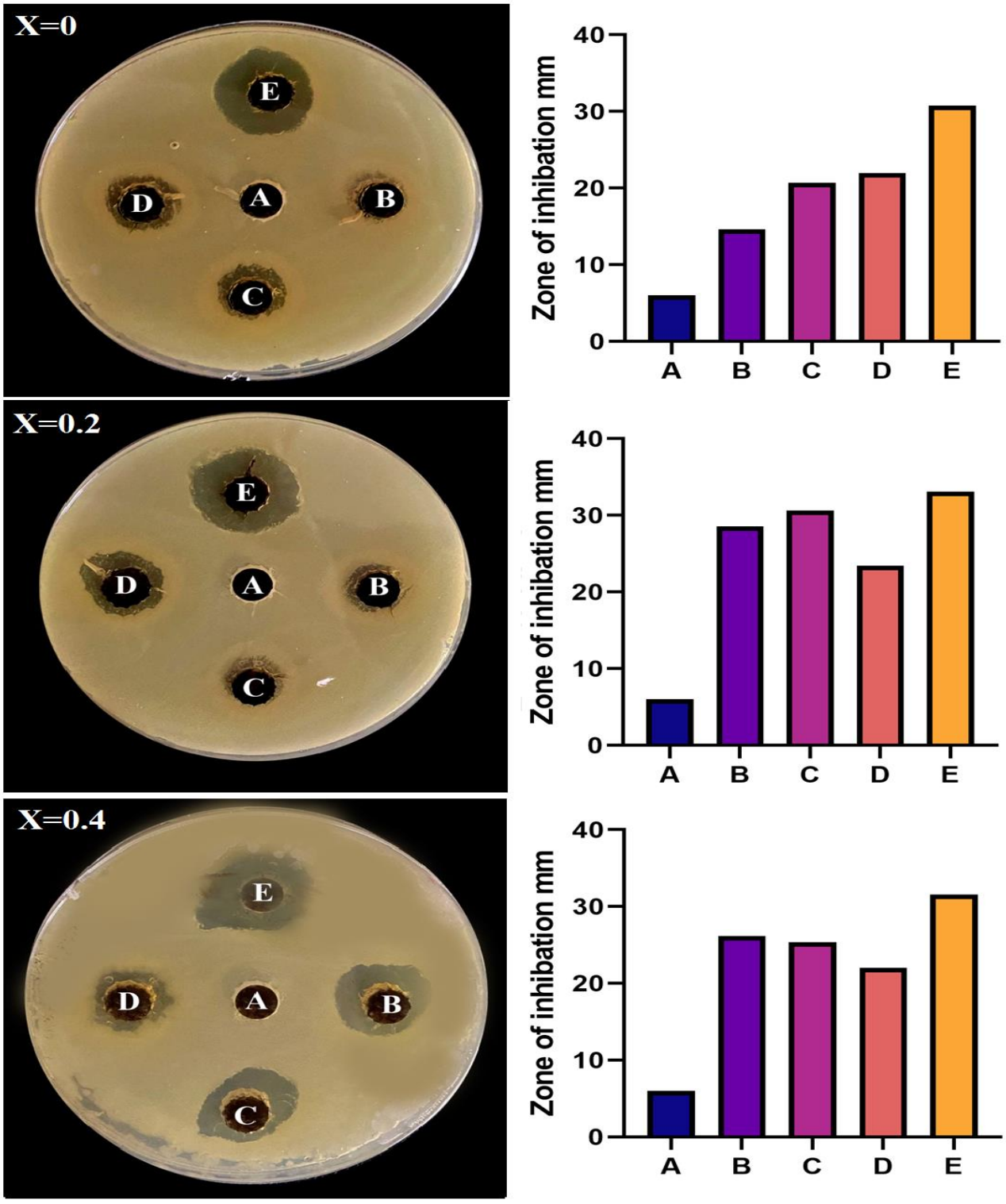

Figure 4.15: Antibacterial activity of $Co_{1-x}Ni_xFe_2O_4$ thin films at different Ni content against *E. coli.* A, control. B, 25%. C, 50%. D, 75%. E, 100%.

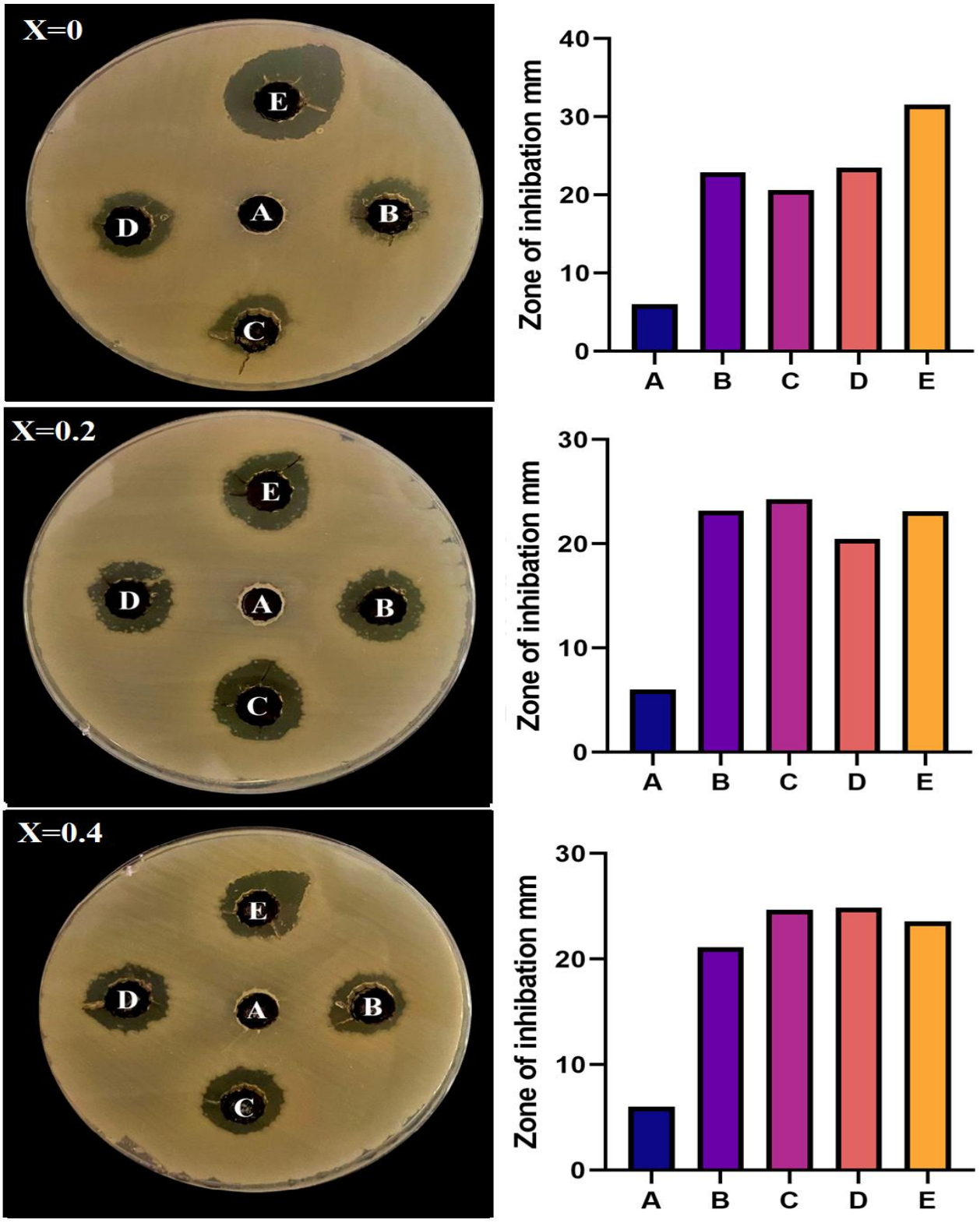

Figure 4.16: Antibacterial activity of $Co_{1-x}Ni_xFe_2O_4$ thin films at different Ni content against *S. aureus*. A, control. B, 25%. C, 50%. D, 75%. E, 100%.

The results demonstrates that the better inhibition of the bacterial growth for Gram-positive compared with the Gram-negative. This result due to the variation in bacterial wall structure. Gram-negative bacteria has a lipid-bilayer membrane, which gives them higher resistance to NPs [113].

The examination showed that all samples had good antibacterial activity. The bacteria-killing process can be explained by different mechanisms: The antibacterial activity of metal ions (Ni^{2+}, Co^{2+}, and Fe^{3+}) liberated from samples that penetrate the bacteria cell and have toxic nature, oxidative stress, damage to cell membranes after contact with their surface, proteolysis, or the combination of all these factors [105], [114].

The created nanoparticles candidate could be used in drug delivery systems, as its magnetic and antibacterial properties [107]. While, the resultant magnetic thin film with antibacterial behavior is candidate for exploring applications in micro-electromagnetic systems such as micropumps, and robots [115].

4.7 Conclusions

In this work, $Co_{1-x}Ni_xFe_2O_4$ powders were prepared by the co-precipitation method and thin films by pulsed laser deposition technique at different ratios.

- The XRD patterns confirm the cubic spinel structure. Same peaks of Spinal phase appeared in thin film samples but with less crystallinity. The broad feature for diffraction lines in thin films (broader than powder samples) indicates a nano-crystalline structure. The crystalline size measured using the Scherrer equation for a thin film is less than for powder samples
- The lattice constant, cell volume, density, and ion jump lengths (LA and LB) decreased with the Ni substitution, which in turn highly affects the magnetic properties of the samples.
- The FTIR indicates the formation of ferrite structure and shows an increase in the frequency of vibration corresponding to site A and site B with the Ni content
- The magnetic properties have a good correlation with the structural parameters of the spinal structure.
- The samples showed good antibacterial activity, especially against gram-positive bacteria.
- The (Ni-Co)Fe_2O_4 powder obtained in this work can be a candidate against different pathogens, preventing bacterial infection. Therefore, if these are coatings on different surfaces, the prepared metal ferrite thin films can be used in biological applications to prevent bacterial spreading. The prepared magnetic nanoparticles are a candidate for use as a drug delivery agent. The properties of the prepared metal ferrite NPs strongly dependent upon the method of synthesis and extremely dependent on the nickel substitution.

4.8 Future Scope of the work

The scopes of the future works are proposed as:

1. Sol-gel auto combustion method could be used to synthesize cobalt- nickel ferrite nanoparticles at a temperature higher than room temperature.
2. A study at different temperatures could be done to determine the influence of temperature on cobalt-nickel ferrite formation.
3. Using Co-Ni ferrite nanoparticles treatment of cancer patients.

References

Reference

[1]. B. D. Cullity and C. D. Graham, "introduction to magnetic materials", 2nd Ed, John Wiley and Sons, ch.6, 175-196, (2009).

[2]. A. Goldman, *" Modern ferrite technology*" Springer Science & Business Media, (2006).

[3]. Y. Xiao, J. Du, "Superparamagnetic nanoparticles for biomedical applications" *Journal of Materials Chemistry, B*, *8*(3), 354-367, (2020).

[4]. N. Ed. Huilgol, *"* Hyperthermia" Bod–Books on Demand, (2013).

[5]. W. Günther, P. Winkler, "A user guide to soft magnetic materials" *lFe*, *1*, 1], (2018).

[6]. A. B. Shinde," Structural and electrical properties of cobalt ferrite nanoparticles*" Int J Innov Technol Explor Eng*, *3*(4), (2013).

[7]. B. D. Cullity, " Introduction to magnetic materials*" New Jersey: Addison-Wiley Publishing Company*, (1972).

[8]. Ahmed, M. A. A. ,"A review on the properties and uses of ferrite magnet" Doctoral dissertation, Sudan University of Science and Technology,(2017).

[9]. M. J. Iqbal, Z. Ahmad,*"* Electrical and dielectric properties of lithium manganate nanomaterials doped with rare-earth elements. *Journal of Power Sources*" *Journal of Power Sources*, *179*(2), 763-769, (2008).

[10]. M. Houshiar, F. Zebhi, Z. J. Razi, A. Alidoust, Z. Askari, "Synthesis of cobalt ferrite ($CoFe_2O_4$) nanoparticles using combustion, coprecipitation, and precipitation methods: A comparison study of size, structural, and magnetic properties" *Journal of Magnetism and Magnetic Materials*, *371*, 43-48, (2014).

[11]. M.S. Khandekar, R.C. Kambale, J.Y. Patil, Y.D. Kolekar, S.S. Suryavanshi, " Effect of calcination temperature on the structural and

electrical properties of cobalt ferrite synthesized by combustion method" Journal of Alloys and compounds, 509(5), pp.1861-1865, (2011).

[12]. R. Lotfi, P. Derakhshi, S.A. Khorramie, "Effect of temperature on synthesis and morphology of nickel doped cobalt ferrite in presence of htab by co-precipitation route" World Appl Sci J, 18(7), pp.929-32,)2012(.

[13]. M. L. Mane, V. N. Dhage, S. E. Shirsath, R. Sundar, K. Ranganathan, S. M. Oak, K. M. Jadhav, ″ Nd: YAG laser irradiation effects on the structural and magnetic properties of polycrystalline cobalt ferrite" , *Journal of Molecular Structure 1035*, 27-30, (2013).

[14]. M. Mozaffari, J. Amighian, E. Darsheshdar," Magnetic and structural studies of nickel-substituted cobalt ferrite nanoparticles, synthesized by the sol–gel method″ *Journal of Magnetism and Magnetic materials, 350*, 19-22, (2014).

[15]. M. Raza , Y.Jamil, F. Jabeen andT.Hussain " A novel laser assisted structure refinement of $Co_{0.5}Zn_{0.5}Fe_2O_4$ " Laser Phys. Lett. ,Vol.11 , p.p (046002-7) ,(2014).

[16]. I. Zalite, G. Heidemane, L. Kuznetsova, M. Maiorov, ″ Hydrothermal synthesis of cobalt ferrite nanosized powders" In *IOP Conference Series:* Materials Science and Engineering (Vol. 77, No. 1, p. 012011). IOP Publishing, (2015).

[17]. T. Yadavalli, H. Jain, G.Chandrasekharan, and R. Chennakesavulu. " Magnetic hyperthermia heating of cobalt ferrite nanoparticles prepared by low temperature ferrous sulfate based method " Aip Advance ,Vol.6,p.p 055904(1-6), 2016.

[18]. Gibin, S. R., & Sivagurunathan, P. (2017). Synthesis and characterization of nickel cobalt ferrite (Ni1− xCoxFe2O4) nano particles by co-precipitation method with citrate as chelating agent. *Journal of Materials Science: Materials in Electronics*, *28*(2), 1985-1996..

[19]. S. Sagadevan, Z. Z. Chowdhury, R. F. Rafique, "Preparation and characterization of nickel ferrite nanoparticles via co-precipitation method. *Materials Research"*, *21*, (2018).

[20]. M. Arshad, M. Asghar, M. Junaid, M. F. Warsi, M. N. Rasheed, M. Hashim, M. A. Khan, " Structural and magnetic properties variation of manganese ferrites via Co-Ni substitution″ Journal of Magnetism and Magnetic Materials, 474, 98-103, (2019).

[21]. M. Kishimoto, H. Latiff, E. Kita, H. Yanagihara, " Structure and Magnetic Properties of Co–Ni Spinel Ferrite Particles Synthesized via Co-Precipitation and Hydrothermal Treatment at Different Temperatures″ Materials transactions, *60*(4), 485-489, (2019).

[22]. S. V. Bhandare, R. Kumar, A. V. Anupama, M. Mishra, R. V. Kumar, V. M. Jali, B. Sahoo, " Effect of Mg-substitution in Co–Ni-Ferrites: Cation distribution and magnetic properties*", Materials Chemistry and Physics*, *251*, 123081, (2020).

[23]. S. M. A. Ridha, H. A. Khader, " XRD and SEM characteristics of Co-Ni ferrite nanoparticles Synthesized using sol-gel method*", Turkish Journal of Computer and Mathematics Education (TURCOMAT) 12*(14), 675-687, (2021).

[24]. S. U. Durgadsimi, V. R. Kattimani, N. S. Maruti, A. B. Kulkarni, S. N. Mathad, "SYNTHESIS AND STRUCTURAL ANALYSIS OF NICKEL FERRITE SYNTHESIZED BY CO-PRECIPITATION METHOD".

[25]. J. Wallyn, N. Anton, T. F. Vandamme, " Synthesis, principles, and properties of magnetite nanoparticles for in vivo imaging applications" A review. *Pharmaceutics*, *11*(11), 601, (2019).

[26]. L. X. Tiefenauer, G. Kuehne, R. Y. Andres, " Antibody-magnetite nanoparticles: in vitro characterization of a potential tumor-specific contrast agent for magnetic resonance imaging", *Bioconjugate chemistry4*(5), 347-352, (1993).

[27]. Jordan, A., Scholz, R., Wust, P., Fähling, H., Krause, J., Wlodarczyk, W., ... & Felix, R. Effects of magnetic fluid hyperthermia (MFH) on C3H mammary carcinoma in vivo. *International Journal of Hyperthermia*, *13*(6), 587-605, (1997).

[28]. C. S. Kumar, F. Mohammad," Magnetic nanomaterials for hyperthermia-based therapy and controlled drug delivery"*Advanced drug delivery reviews*, *63*(9), 789-808, (2011).

[29]. M. Colombo, S. Carregal-Romero, M. F. Casula, L. Gutiérrez, M. P. Morales, I. B. Böhm, W. J. Parak, " Biological applications of magnetic nanoparticles", *Chemical Society Reviews 41*(11), 4306-4334, (2012).

[30]. IM, M. B. "Preparation and Characterization of Magnetic Glass Ceramics Derived from Iron Oxides Bearing Rolling Mill Scales Wastes". *Nano Research*, *1*(1), 6. (2015).

[31]. A. T. Pathan and A. M .Shaikh, "Synthesis and characterization of cobalt substituted Ni-Zn nano ferrites by chemical route", Scholars Research Library, **V.**4, p.p173-178, (2012).

[32]. M. Niyaifar, H. Shalilian, A. Hasanpour, H. Mohammadpour, "Effect of copper substitution on structural and magnetic properties of NiZn ferrite nanopowders" *Journal of Magnetics*, *18* (4), 391-394, (2013).

[33]. K. J. Standley, " Oxide Magnetic Materials" Oxford University Press, (1972).

[34]. A. Goldman, " Modern Ferrite Technology" New York: Van Nostrand Reinhold, (1990).

[35]. A. Nicola Spaldn, "Magnetic Materials: Fundamentals and Device Applications" Cambridge University Press (2003).

[36]. J. Smit, H.P.J. Wijn, Ferrites, Jhon Wiley and Sons, NewYork, (1959).

[37]. Ortiz-Quiñonez, J. L., Pal, U., & Villanueva, M. S. Structural, magnetic, and catalytic evaluation of spinel Co, Ni, and Co–Ni ferrite nanoparticles fabricated by low-temperature solution combustion process. ACS omega, 3(11), 14986-15001, (2018).

[38]. M. Hua, S. Zhang, B. Pan, W. Zhang, L. Lv, Q. Zhang. " Heavy metal removal from water/ wastewater by nanosized metal oxides" J Hazard Mater211–212: 317–31, (2012).

[39]. R. Ali, A. Mahmood, M.A. Khan, A.H. Chughtai, M. Shahid, I. Shakir, " Impacts of Ni– Co substitution on the structural, magnetic and dielectric properties of magnesium nano-ferrites fabricated by micro-emulsion method" J Alloys Compd;584: 363–8, (2014).

[40]. Z.R. Dai, Z.W. Pan, Z.L. Wang. " Novel nanostructures of functional oxides synthesized by thermal evaporation" Adv Funct Mater 13(1):9–24, (2003).

[41]. I. Hilger, W.A. Kaiser, " Iron oxide-based nanostructures for MRI and magnetic hyperthermia" Nanomedicine 7(9):1443–59, (2012).

[42]. W. Wei, W. Zhaohui, Y. Taekyung, J. Changzhong, K. Woo-Sik " Recent progress on magnetic iron oxide nanoparticles: synthesis, surface functional strategies and biomedical applications" Sci Technol Adv Mater 16(2):023501, (2015).

[43]. N.T. Lan, N.P. Duong, T.D. Hien, " Influences of cobalt substitution and size effects on magnetic properties of coprecipitated Co–Fe ferrite anoparticles" J Alloys Compd 509(19):5919–25, (2011).

[44]. Beji, Z., Sun, M., Smiri, L. S., Herbst, F., Mangeney, C., & Ammar, S. Polyol synthesis of non-stoichiometric Mn–Zn ferrite nanocrystals: structural/microstructural characterization and catalytic application. *RSC advances*, *5*(80), 65010-65022, (2015).

[45]. Beji, Z., Sun, M., Smiri, L. S., Herbst, F., Mangeney, C., & Ammar, S. Polyol synthesis of non-stoichiometric Mn–Zn ferrite nanocrystals: structural/microstructural characterization and catalytic application. *RSC advances*, *5*(80), 65010-65022, (2015).

[46]. A. S. Albuquerque, J. D. Ardisson, E. Bittencourt and W.A. Macedo, " Synthesis of iron oxide nanoparticles under oxidizing environment and their stabilization in aqueous and non-aqueous media" J. Materials Research,V. 2, p.p235-238, (1999).

[47]. O. Caltun, M. Feder and A. Sava, " Structure and Magnetic Properties of Granular NiZn-Ferrite - SiO_2 "J. Appl. Phys. V. 8,p.p 51- 55, (1999).

[48]. R. Peelamedu, C. Grimes, D. Agrawal, and R. Roy," Ultralow dielectric constant nickel–zinc ferrites using microwave sintering", J. Mater. Res.,V. 18,p.p 2292 -2295, 2003.

[49]. S. A. Morrison, C. L. Cahill, E. E. Carpenter, S. Calvin, R. Swaminathan, M. E. McHenry and V. G. Harris," Magnetic and structural properties of nickel zinc ferrite nanoparticles synthesized at room temperature", J. Appl. Phys., V.95, p.p6392-6395, 2004.

[50]. K. B. Modi, M. K. Rangolia, M. C. Chhantbar and H. H. Joshi," Study of infrared spectroscopy and elastic properties of fine and coarse-grained nickel–cadmium ferrites", J. Mater. Sci.,V. 41, p.p7308–7318, 2006.

[51]. P.K. Roy and J. Bera, " Study of infrared spectroscopy and elastic properties of fine and coarse-grained nickel–cadmium ferrites" Elsevier, V.197, p.p279–283, (2008).

[52]. Tripathi, S. K., Kaur, R., Bharti, S., Gawri, I., & Kaur, J. Recent advances in synthesis, properties and applications of magnetic oxide nanomaterials. Solid State Phenomena, 232, 1-44 (2015).

[53]. W. D. Kingery, H. K. Bowen, and D. R. Uhlmann, "Cation distribution of $Co_{0.5}Zn_{0.5}Fe_2O_4$ nanoparticles" Introduction to ceramics , Wiley New York, (1976).

[54]. J. Crangle, "Solid State Magnetism , Edward Arnold: London", U.K., (1991).

[55]. S. Brian Mitchell, " An Introduction to Materials Engineering and Science for Chemical and Materials Engineers" John Wiley Sons, (2004).

[56]. D. L. Leslie-Pelecky, R. D. Rieke, " Magnetic properties o nanostructured materials" Chemistry of materials, vol. 8, no. 8, pp. 1770- 1783, (1996).

[57]. D. Gubbins, E. Herrero-Bervera, " , Encyclopedia of geomagnetism and paleomagnetism " Springer, Berlin, (2007).

[58]. S.V. Ganachari, N.R. Banapurmath, B. Salimath, J.S. Yaradoddi, A.S. Shettar, A.M. Hunashyal, A. Venkataraman, P. Patil, H. Shoba and G.B. Hiremath, " Synthesis techniques for preparation of nanomaterials" Handbook of Ecomaterials, Springer, Cham. https://doi. org/10.1007/978-3-319-48281- 1_149-1,)2017(.

[59]. O. Tünay, N.I., Kabdaşli, " Hydroxide precipitation of complexed metals " Water Research, 28(10), pp.2117-2124,)1994(.

[60]. E. K. Hamed, F. Hattab, and M. Fakhry, " Laser wavelength and energy effect on optical and structure properties for nano titanium oxide prepared by pulsed laser deposition" Iraqi J. Phys., vol. 12, no. 25, pp. 62–68,)2014(.

[61]. S. R. Mohanty, P. Lee, T. L. Tan, S. V. Springham, A. Patran, R. V. Ramanujan, and R. S. Rawat. " Effect of deposition parameters on morphology and size of FeCo nanoparticles synthesized by pulsed laser ablation deposition " *Applied surface science* 252, no. 8 2806-2816, (2006).

[62]. S. Beke, S. Giorgio, L. Korosi, L. Nanai, and W. Marine, " Structural and optical properties of pulsed laser deposited V_2O_5 thin films" Thin Solid Films, vol. 516, no. 15, pp. 4659–4664,)2008(.

[63]. A. A. Yousif and M. H. Hasan, " Growth of Nanostructured CdO : In Films by Pulsed Laser Deposition" IRAQI J. Appl. Phys., vol. 11, no. 1, pp. 15–19,)2015(.

[64]. J. Zhang, J. Claverie, M. Chaker, and D. Ma, “Colloidal Metal Nanoparticles Prepared by Laser Ablation and their Applications,” ChemPhysChem, vol. 18, no. 9, pp. 986–1006,)2017(.

[65]. Ugandhar, S., Gupta, M., & Sinha, S. K. (2006). Enhancing strength and ductility of Mg/SiC composites using recrystallization heat treatment. *Composite structures*, *72*(2), 266-272.

[66]. D. William, "material science and engineering an introduction" John wiley &son , Inc , p.676-681, (2000).

[67]. B.G. Street, "Present technology of hard and soft ferrites". Powder Metallurgy, 22(2), pp.62-74, (1979).

[68]. Z.M.A Hamandi, K.A. Al-Khazraj, " Predictors of In-Hospital Mortality After Acute Myocardial Infarction" The Iraqi Postgraduate Medical Journal VOL.10, (2011).

[69]. P.U. Heuschmann, D. Neureiter, M. Gesslein, B. Craiovan, M. Maass, G. Faller, G. Beck, B. Neundoerfer, P.L. Kolominsky-Rabas, " Association between infection with helicobacter pylori and chlamydia pneumoniae and risk of ischemic stroke subtypes: results from a population-based case–control study" Stroke. Vol.32 pp.2253– 2258, (2001).

[70]. S. M. Holland, C. A. Gaydos, T. C. Quinn," Detection and differentiation of Chlamydia trachomatis, Chlamydia psittaci, and Chlamydia pneumoniae by DNA amplification" J. Infect. Dis". 162:984–987, (1990).

[71]. H. Chang, S. Shu-Qing, " Silicon nanoparticles :Preparation properties, and application intrnat" .Conference nanosci.& technol.,Vol.23, 088102, (2014).

[72]. K.Taeho B.B. Gary, S. Zhi-gang, H. Sazid, R. Erkki, J.S. Michael," Composite Porous Silicon-Sliver Nanoparticles as Theranostic Antibacterial Agents" ACS. Appl. Mater. Interfaces,1-27, (2016).

[73]. R.J. Martin-Palma, M. Manso-silvan, V. Torres-Costa, " Biomedical applications of nanostructured porous silicon: Rev" J. Nanophot Vol. 4, pp.1-20, (2010).

[74]. N.A. Hoseini, M. Shahtahmasebi, M. Rezaee-Roknabadi, M.M. Mashreghi, E.A. Bagher-Mohagheghi P. Madahi, " Fabrication of CuO:Fe nanoparticles by Sol-Gel Method and Study and Structural and Antibacterial Properties" 2n .Confe. Appl. Nanotechnol. Sci. Engin.Medi.,1-2, (2011).

[75]. F. Von Nussbaum, M. Brands, B. Hinzen, S. Weigand, D. Habich," Antibacterial natural products in medicinal chemistry-Exodus or revival" Chem.Int.Ed. Vol.45, pp.5072-5129, (2006).

[76]. R. Ahmad, M. Sardar," TiO_2 Nanoparticles as an antibacterial Agents Against E.Coli" Inter. J. Inn. Rese. Sci., Eng. Technol., Vol. 2, pp.3569-3574, (2013).

[77]. S. Rezaei-Zarchi, A. Javed, M.J. Ghani, S.Soufian, F.B. Firouzabadi, A.B. Moghaddam, S.H. Mirjalili," Comparative Study of Antimicrobial Activities of TiO_2 and CdO nanoparticles against the pathogenic strain of Escherichia coli" Iran. J. Path., Vol. 5, pp. 83-89, (2010).

[78]. A. Stoyanova, H. Hitkova, A. Bachvarova-Nedelcheva," Synthesis and Antibacterial Activity of Tio2/Zno Nanocomposites Prepared via Nonhydrolytic Route" J. Chem. Technol. Met., Vol.48 , pp.154-161, (2013).

[79]. T.M., Al-Nori " Antibacterial activity of Silver and Gold Nanoparticles Against Streptococcus, staphylococcus aureus andE.coli "Al-Must. J. Sci.,Vol. 23, pp.45-54, (2012).

[80]. M. Akhtar, M.k. Swamy, A. Umar, A. Sahli, A. Abdullah," Biosynthesis and characterization of silver nanoparticles from methanol leaf extract of cassia didymobotyra and assessment of their antioxidant and antibacterial activities" J. Nan.Nanotechnol., Vol. 15, pp. 9818-9823, (2015).

[81]. I.Y. Wong, S.N. Bhatia and M. Toner, " Nanotechnology: Emerging tools for biology and medicine" Gen. Dev., Vol. 27, pp. 2397-2408, (2013).

[82]. M. Jena, S. Mishra, S. Jena, S. S. Mishra, "Nanotechnology-future prospect in recent medicine: A review", (2013)..

[83]. M. Ajmal, *" Fabrication and Physical Characterization of* *$Ni_{1-x}Zn_xFe_2O_4$ and $Cu_{1-x}Zn_xFe_2O_4$ Ferrites* " (Doctoral dissertation, Quaid-i-Azam University Islamabad, Pakistan), (2008).

[84]. B. D. Cullity, "Chemical analysis by X-ray diffraction. *Elements of X-ray diffraction"*, 397-420, (1978).

[85]. K.L. Horovitz, V.A. Johnson. "*Solid State Physics"*, vol. 6, Academic Press, New York and London, (1959). .

[86]. R. Sharma, D. P. Bisen, U. Shukla, B. G. Sharma, " X-ray diffraction: a powerful method of characterizing nanomaterials*"*, *Recent research in science and technology 4*(8), (2012).

[87]. B.D. Cullity, S.R. Stock, " Elements of X-Ray Diffraction , Third Edition" Third Edition, Pearson Education Limited, (2014).

[88]. E. W. Nicodemus, "Introduction to Advanced X-ray Diffraction Techniques for Polymeric Thin Films, Coatings", vol.6, no.4:54, pp.1-17, (2016).

[89]. L. A. Henrik, S. M. Matilde, " Crystalline and magnetic structure-property relationship in spinel ferrite nanoparticles" Nanoscale, vol.10, no.31, pp. 14902-14914, (2018).

[90]. M. Ali Mohammad, M. A. R. Sabah, H. M. Tahseen, " Dielectric Properties Of Cr-Substituted Cobalt Ferrite Nanoparticles Syntheses by Citrate-Gel Auto Combustion Method" International Journal Of Applied Engineering Research, vol.13, no.8, pp.6026-6035, (2018).

[91]. W.Yoshio, M. Eiichiro and K. Shinoda, " X-Ray Diffraction Crystallography : introduction, examples and solved problems "Springer Science and Business Media, (2011).

[92]. M. S.J. Kanchan, A. S.Yogesh, A. A .Anuradha, B. S .Hiralal, P. R. Suresh, P. P. Rajendra, R. Patil, B. B. Kale, G. M. Chaskar, Mediated Biosynthesis of ZnO and TiO_2 Nanocomposites for Enhanced Antimicrobial Activity "Journal of Composites Science", vol.3, no.3:90, (2019).

[93]. N. S. Ahmade "Synthesis and Magnetic Characterization of $Co_xZn_{1-x}Fe_2O_4$ Spinel Ferrite nano Particles for Biological Applications "Phd , University of Technology, (2019).

[94]. A. S. H. Makhlouf, and A. Barhoum, " Emerging Applications of Nanoparticles and Architectural Nanostructures" Current Prospects and Future Trends: William Andrew, (2018).

[95]. T. Zhou, D. Zhang, L. Jia, F. Bai, L. Jin, Y. Liao, T. Wen, C. Liu, H. Su, N. Jia, Z. Zheng, " Effect of NiZn ferrite nanoparticles upon the structure and magnetic and gyromagnetic properties of low-temperature processed LiZnTi ferrites" The Journal of Physical Chemistry C, 119(23), pp.(13207- 13214,) (2015).

[96]. Roovers, J. Encyclopedia of polymer science and engineering. *Mark, HF*, 478,(1985).

[97]. J. L. Ortiz-Quiñonez, U. Pal, M. S. Villanueva, "tructural, Magnetic, and Catalytic Evaluation of Spinel Co, Ni, and Co−Ni Ferrite Nanoparticles Fabricated by Low-Temperature Solution Combustion Process*" ACS Omega*, vol. 3, p. 14986−15001, (2018).

[98]. F. Tudorache, P. D. Popa, M. Dobromir, F. Iacomi, "tudies on the structure and gas sensing properties of nickel–cobalt ferrite thin films prepared by spin coating*"Materials Science and Engineering: B*, *178*(19), 1334-1338, (2013).

[99]. K. Jalaiah, K. C. Mouli, K. V.Babu, R. V. Krishnaiah, " Structural, electrical and magnetic properties of Mg-Zr co-substituted Ni0. 5Zn0. 5Fe2O4" *Journal of Science: Advanced Materials and Devices"*, *4*(2), 310-318, (2019).

[100]. A. R., Chavan, R. R., Chilwar, P. B., Kharat, K. M. Jadhav, " Effect of annealing temperature on structural, morphological, optical and

magnetic properties of NiFe2O4 thin films" *Journal of Superconductivity and Novel Magnetism*, *31*(9), 2949-2958, (2018).

[101]. R. Tiwari, M. De, H. S.Tewari, S. K. Ghoshal," Structural and magnetic properties of tailored NiFe2O4 nanostructures synthesized using auto-combustion method" *Results in Physics*, *16*, 102916, (2020).

[102]. O. Abd-Elkader, A. M. Al-Enizi, S. F. Shaikh, M. Ubaidullah, M. O. Abdelkader, N. Y. Mostafa, " The Structure, Magnetic, and Gas Sensing Characteristics of W-Substituted Co-Ferrite Nanoparticles", *Crystals 12*(3), 393, (2022).

[103]. H. Kumar, J. P. Singh, R. C. Srivastava, P. Negi, H. M. Agrawal, K. Asokan, " FTIR and electrical study of dysprosium doped cobalt ferrite nanoparticles" *Journal of Nanoscience*, (*2014)*.

[104]. Y. Iqbal, H. Bae, I. Rhee, S. Hong, " Relaxivities of hydrogen protons in aqueous solutions of PEG-coated rod-shaped manganese-nickel-ferrite (Mn0. 4Ni0. 6Fe2O4) nanoparticles" *Journal of the Korean Physical Society*, *65*(10), 1594-1597, (2014).

[105]. S. Munir, M. F. Warsi, S. Zulfiqar, I. Ayman, S. Haider, I. A. Alsafari, I. Shakir, " Nickel ferrite/zinc oxide nanocomposite: Investigating the photocatalytic and antibacterial properties" *Journal of Saudi Chemical Society*, *25*(12), 101388, (2021).

[106]. M. S. Lashkenari, M. Ghorbani, H. Naghibi, P. Khalaj, S" Synthesis and characterization of polyrhodanine/nickel ferrite nanocomposite with an effective and broad spectrum antibacterial activity" *Polymer-Plastics Technology and Materials 58*(13), 1461-1470, (2019).

[107]. S. C. Watawe, V. Mujumdar, R. S. Chaughule, "Nanotechnology in Drug Administration and Food", (2009).

[108]. M. Hashim, S. Kumar, S. E. Shirsath, R. K. Kotnala, J. Shah, R. Kumar, " Synthesis and characterizations of Ni^{2+} substituted cobalt ferrite nanoparticles" *Materials Chemistry and Physics*, *139*(2-3), 364-374, (2013).

[109]. P. Jing, J. Du, C. Jin, J. Wang, L. Pan, J. Li, Q. Liu," Improved coercivity and considerable saturation magnetization of cobalt ferrite (CoFe2O4) nanoribbons synthesized by electrospinning" *Journal of materials science 51*(2), 885-892, (2016).

[110]. P. A. Shaikh, R. C. Kambale, A. V. Rao, Y. D. Kolekar, " Structural, magnetic and electrical properties of Co–Ni–Mn ferrites synthesized by co-precipitation method" *Journal of Alloys and Compounds*, *492*(1-2), 590-596, (2010).

[111]. G. Dixit, J. P. Singh, R. C. Srivastava, H. M. Agrawal, R. J. Chaudhary, " Structural, magnetic and optical studies of nickel ferrite thin films", *Adv. Mater. Lett3*(1), 21-26, (2012).

[112]. M. Oujja, L. Martín-García, E. Rebollar, A. Quesada, M. A. García, J. F. Fernández, M. Castillejo, " Effect of wavelength, deposition temperature and substrate type on cobalt ferrite thin films grown by pulsed laser deposition *" Applied Surface Science 452*, 19-31,(2018).

[113]. M. Kooti, S. Gharineh, M. Mehrkhah, A. Shaker, H. Motamedi, " Preparation and antibacterial activity of CoFe2O4/SiO2/Ag composite impregnated with streptomycin" *Chemical Engineering Journal*", *259*, 34-42, (2015).

[114]. K. L. Rincón-Granados, A. R. Vázquez-Olmos, A. P. Rodríguez-Hernández, A. Vega-Jiménez, F. Ruiz, V. Garibay-Febles, L. A. Ximénez-Fyvie, " Facile solid-state synthesis and study in vitro of the antibacterial activity of NiO and NiFe2O4 nanoparticles *"Materialia*, *15*, 100955, (2021).

[115]. D. Ficai, M. Gheorghe, G. Dolete, B. Mihailescu, P. Svasta, A. Ficai, E. Andronescu," Microelectromechanical Systems Based on Magnetic Polymer Films*" Micromachines, 13*(3), 351, (2022).

الخلاصة:

في هذه الدراسة حضرت الجسيمات النانوية المغناطيسية بصيغة $Co_{1-x}Ni_xFe_2O_4$ بطريقتين. الأولى الترسيب المشترك, الطريقة الأخرى هي طريقة الترسيب بالليزر النبضي. استخدم خليط من نترات النيكل ونترات الكوبلت و نترات الحديد وكذلك هيدروكسيد الصوديوم كعامل قوي للتحكم بمقدار الاس الهايدروجيني .

العينات التي حضرت بطريقة الترسيب المشرك حرقت بدرجة حرارة 300 درجة سليزية لمدة ثلاث ساعات لإزالة محتوى الماء والشوائب غير المرغوب فيها وللحصول على هيكل سبينيل أحادي الطور أفضل. ثم بعد ذلك ضغط المسحوق ليحول الى قرص (2) سم لغرض تشعيعه بطاقة ليزر 600 ملي جول لتحويله الى غشاء رقيق

تم أختبار الخصائص التركيبية والمغناطيسية للنماذج بأستعمال حيود الأشعة السينية XRD،المطياف الألكتروني للمجال المنبعث FE-SEM، تحويلات فورير لمطيافية الأشعة تحت الحمراء FTIR، وأخيراً مطياف الرنين المغناطيسي VSM. يُظهر طيف الأشعة السينية أن نمط الجسيمات المتكونة هو النمط المكعب المتمركز الأوجه وتم حساب القيم النظرية لثابت الشبيكة،والحجم البلوري D حيث يقع الحجم البلوري المحسوب في المدى (22.6-25.2 نانومتر) ، إما في طريقة الترسيب بالليزر النبضي في المدى (13.4-13.7 نانومتر).

تُظهر تحويلات فورير لمطيافية الأشعة تحت الحمراء FTIR وجود حزمتي أمتصاص تتراوح ضمن المدى 400 – 600 سم$^{-1}$. تشير هذه الحزم أن تركيب الطيف لجميع النماذج هو الفيرايت.

أكد فحص (FE-SEM) أن طرق التحضير أنتجت جسيمات نانوية كروية مع تغيير طفيف في توزيع حجم الجسيمات. يقدر متوسط حجم الجسيمات بواسطة الترسيب المشترك بحوالي 23 نانومتر ومتوسط حجم الجسيمات عن طريق طريقة الترسيب بالليزر النبضي (PLD) يقدر بحوالي 20 نانومتر بأستخدام برنامج(Imag J).

اضهرت نتائج قياس المغناطسية لاهتزاز العينة(VSM) ان للخصائص المغناطيسيه علاقة جيدة مع المعلمات الهيكلية للبنية الاسبنل ، والتي زادت مع محتوى النيكل,أظهرت كل من عينات الباودر و (PLD) شكل حلقة تخلف ضيقه . بعض العينات اظهرت سلوك مواد فائقة المغناطيسية.

عند أستخدام الجسيمات النانوية المحضرة بطريقه الترسيب المشترك على انواع من البكتريا بكتريا الـ *S.aureus bacteria,* *Escherichia coli* وُجد أن اعلى نطاق التثبيط لبكتريا الـ S.aureus bacteriaتراوح ضمن 27 – 33 ملم أما لبكتريا (*Escherichia coli*) تتراوح ضمن 30 ملم .

اما عند استخدام الجسيمات النانوية المحضرة بطريقه الترسيب بالليزر النبضي على نفس الانواع من البكتريا وجد ان بكتريا (S.aureus bacteria) قد سجلت اعلى نسبة تثبيط تتراوح مابين(22-32ملم) أما لبكتريا (*Escherichia coli*) تتراوح ضمن 27-30 ملم .

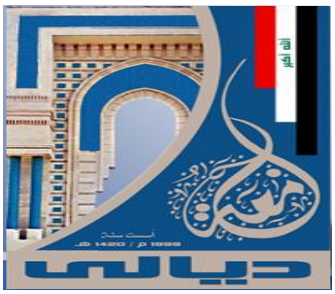

جمهورية العراق

وزارة التعليم العالي والبحث العلمي

جامعة ديالى

كلية العلوم

قسم الفيزياء

تحسين الخصائص المغناطيسية لجسيمات (كوبلت- نيكل) فرايت النانوية بواسطة الترسيب بالليزر النبضي و دراسة تأثيره البيولوجي

رسالة مقدمة الى

درجة وهي جزء من متطلبات نيل مجلس كلية العلوم – جامعة ديالى الفيزياء الماجستير في علوم

من قبل

مروه حازم صبار

بكالوريوس علوم فيزياء 2019 م

بإشراف

أ.د.تحسين حسين مبارك

أ.م.د.ندى سهيل احمد

1444 هـ

2022م